# The Stationary Wave Response to a Midlatitude SST Anomaly in an Idealized GCM

MINGFANG TING

*Cooperative Institute for Research in Environmental Sciences, University of Colorado at Boulder, Boulder, Colorado*

(Manuscript received 31 August 1990, in final form 3 December 1990)

ABSTRACT

The atmospheric stationary wave response to a midlatitude sea surface temperature (SST) anomaly is examined with an idealized general circulation model (GCM) as well as steady linear model, in a similar way as Ting and Held, for a tropical SST anomaly. The control climate of the GCM is zonally symmetric; this symmetric climate is then perturbed by a monopole SST anomaly centered at 40°N.

Two experiments, with SST anomalies of opposite sign, have been conducted. The stationary response is roughly linear in the sign of the SST anomaly, despite the fact that precipitation shows strong nonlinearity. The linear model, which is an exact linearization of the GCM equations in use, when forced by anomalous heating and transients, reproduces the GCM's stationary response excellently. The low-level transient eddy heat fluxes act to damp the lower level temperature signal. When this damping effect is mimicked by a horizontal thermal diffusion in the linear model, the response to the diabatic heating alone gives a reasonably good simulation of the GCM's anomaly; the effect of the anomalous transient momentum fluxes is relatively small.

A crude latent heat parameterization scheme, using an evaporation anomaly that is proportional to the mean air–sea surface moisture difference and including the effects of mean moisture advection, is developed. When the perturbation mixing ratio is approximated by assuming fixed relative humidity and by linearizing the Clausius–Clapeyron equation, the linear model's response, utilizing this latent heat parameterization scheme, gives a useful fit to the GCM's anomalous flow.

## 1. Introduction

There have been numerous general circulation model (GCM) and simple mechanistic modeling studies of the influence of tropical sea surface temperature (SST) anomalies on interannual tropical and extratropical low-frequency variability. However, the influence of in situ midlatitude SST anomalies on the low-frequency extratropical variability has been explored much less thoroughly, at least for the past decade. The use of midlatitude SST anomalies as an indicator for extended long range forecasting is nevertheless a subject with a long history (e.g., Namias 1959, 1963, 1969). Observational studies also show a relation between the northern winter climate anomaly and the midlatitude SST anomaly (e.g., see Namias 1969; Namias and Cayan 1981; Ratcliffe and Murray 1970). It has long been recognized that large-scale air–sea interactions in midlatitudes do play an important role in the variability of both ocean and atmosphere on monthly and seasonal time scales, although opinions about the relative importance of midlatitude and tropical SST's have shifted back and forth over the years. Frankignoul (1985) gives a comprehensive recent review of air–sea feedback processes in midlatitudes.

Recently, observational studies by Wallace and Jiang (1987) and Wallace et al. (1990) found that the patterns of correlation coefficient between the 500 mb geopotential height and midlatitude Pacific and Atlantic SST at certain points are similar to observed atmospheric teleconnection patterns (Fig. 6 of Wallace and Jiang, for example). A similar conclusion was reached by Palmer and Sun (1985) in their analysis of atmospheric patterns associated with SST fluctuations in the region southeast of Newfoundland (Fig. 10 of Palmer and Sun). Wallace and Jiang (1987) further pointed out that the simultaneous correlation between the SST anomalies over the extratropical North Pacific and the large scale circulation anomalies are even stronger than over the El Niño region. Recent GCM modeling results (Palmer and Sun 1985; Pitcher et al. 1987) point in the same direction as the observational evidence. They show that the atmospheric response to a fixed midlatitude SST anomaly is indeed statistically significant and has similar features to the low-frequency atmospheric teleconnection patterns.

The role of midlatitude SST anomalies is examined in this paper by perturbing an idealized GCM with a midlatitude SST anomaly, as in Ting and Held (1990, hereafter refer to as TH) for a tropical SST anomaly. The idealized GCM is designed to have a zonally symmetric control climate. The use of this idealized GCM to study the response to a midlatitude SST anomaly is motivated by previous modeling studies (Palmer and

*Corresponding author address:* Dr. Mingfang Ting, CIRES, University of Colorado, Campus Box 216, Boulder, CO 80309-0216.

Sun 1985; Pitcher et al. 1987), as well as by the tropical SST anomaly experiments with the same idealized GCM (TH). In the tropical SST anomaly experiments, TH found that the storm track behavior is very different in a zonally symmetric environment in comparison to a zonally asymmetric one. The anomalous extratropical transients play a relatively minor role in the zonally symmetric case, in sharp contrast to the result of Held et al. (1989), where diagnosis with a linear model suggests that it is a dominant forcing of the atmospheric response to El Niños. More recently, Lau and Nath (1990, hereafter refer to as LN) carried out a GCM experiment in which both tropical and extratropical SSTs were prescribed in accordance with the observational record over a 30-year period, 1950–79. A regression analysis of selected model parameters versus the SST variations off the Newfoundland coast and northwest of Hawaii reveals that the presence of the SST perturbations in the extratropics is associated with displacements of the storm track axis. The geopotential height anomaly pattern obtained from regression analysis is equivalent barotropically with a spatial structure that is very similar to the observed pattern in Wallace et al (1990). Given the very different transient behavior in a zonally symmetric control climate when perturbed by a tropical SST anomaly (TH), the question remains to be whether a midlatitude SST perturbation would cause significant storm track displacement as in LN, and how the transients feed back to the time mean response.

Furthermore, the scaling arguments in the linear theory by Hoskins and Karoly (1981) point out that a midlatitude shallow heat source is balanced by advection of cooler air from polar regions; thus a trough will be forced about a quarter wavelength downstream of the heat source at low levels. However, the GCM modeling results (Palmer and Sun 1985; Pitcher et al. 1987) with a prescribed midlatitude SST anomaly show the opposite tendency: with a high center being slightly downstream of the warm SST. The GCM experiments also tend to show an equivalent barotropic response, in contrast to the highly baroclinic vertical structure predicted by a linear model. Palmer and Sun try to reconcile the discrepancy by emphasizing the shift of storm track position and the associated anomalous momentum transients, as well as sensible and latent heat release. This speculation is consistent with the results found by LN. Palmer and Sun also emphasize the possible role of the redistribution of heating in the vertical by the transients.

The linear, steady state model developed by Ting (1990) and TH is used to understand the relation between the low level heat source in midlatitudes and the atmosphere's stationary response to this heat source. The relative importance of thermal forcing and forcing by transient eddy momentum flux convergences can also be determined within the linear model framework. Furthermore, the simplicity of the design of the idealized GCM experiments allows one to push this problem further, to relate the midlatitude heat source directly with the SST anomaly. This is the ultimate goal of studies on the atmospheric dynamics of climate anomalies induced by SST anomalies. In a realistic GCM, these problems are much more difficult to solve than in the idealized GCM with a zonally symmetric control climate. As we will see later, even in this relatively simple case, the relation between the atmospheric heating and the SST anomaly is still complex. The relevance of this model's response to a realistic GCM case and to the real atmosphere is still very obscure. Yet we believe this is a very useful starting point toward a better understanding of the more complex systems.

We first discuss the design of the midlatitude SST anomaly experiments in section 2. The GCM's responses to this SST anomaly will be described in section 3. In section 4, linear model diagnoses of the relative importance of diabatic heating and momentum and thermal transients are presented. The moisture budget and some heating parameterization ideas are discussed in section 5. Finally some conclusions are presented in section 6.

## 2. Design of GCM experiments

For the completeness of this paper, we briefly review the design of the control experiment. We use the GFDL Climate Dynamics Group R15 Spectral GCM to carry out all the integrations. The detailed dynamics of this model can be found in Manabe et al. (1979) and Gordon and Stern (1982). It is a global model with 9 sigma levels in the vertical. The model utilizes moist convective adjustment and a semi-implicit time differencing scheme.

We run the model under perpetual January condition. The land–sea mask has been removed and replaced by an all ocean surface. We also take out the sea ice formation and fix the cloud distribution to be zonally symmetric. The ocean surface albedo is fixed at the value of 0.1. A 20-day damping is also included in the top layer of the model to limit the size of the polar night jet, which is very large in the model due to the lack of any large planetary waves in the extratropical stratosphere of this model.

The sea surface temperature is prescribed everywhere on the globe. In the control experiment, it takes the following form,

$$T_s(\theta) = T_0 - T_1 \sin\theta - \frac{2}{3}T_2 P_2(\sin\theta). \qquad (1)$$

Here $\theta$ is latitude; $P_2(x) = \frac{1}{2}(3x^2 - 1)$ is the second Legendre polynomial. When $T_0 = 287$ K, $T_1 = 10$ K, and $T_2 = 40$ K, the control climatology of the idealized GCM with this SST distribution can be found in Fig. 2 of TH.

The zonally symmetric control SST in (1) is then perturbed by a monopole SST anomaly centered at 40°N and 180°E. The following functional form of the SST anomaly has been used:

$$T_A(\lambda, \theta) = Ae^{-[(\theta-40)/L_y]^2-[(\lambda-180)/L_x]^2}. \quad (2)$$

The total SST patterns in the Northern Hemisphere with amplitude $A_\pm = \pm 10$ K, meridional scale $L_y = 15°$, and longitudinal scale $L_x = 30°$ are shown in Figs. 1a and b for positive and negative anomaly cases, respectively. The SST anomaly center is approximately at the latitude of maximum meridional gradient of the zonally symmetric part of the SST and near latitude of the zonally symmetric storm track axis in the control experiment. The position of the maximum meridional gradient of total SST has been shifted about 10° north and south of its control position in the positive and negative anomaly cases, respectively. A midlatitude SST anomaly of amplitude 10 K is much larger than any observed anomalies associated with interannual variability (1 to 2 K). We use stronger forcing in order to unambiguously isolate the climate signal from the weather noise. However, as one will see later, the anomalous responses are approximately linear in the amplitude of the SST anomaly; that is, the response to the negative anomaly is similar to the response to the positive anomaly, but with opposite sign. (The Clausius–Clapeyron equation introduces nonlinearity in evaporation and precipitation anomalies, but not in stationary wave responses, as emphasized below.) Thus one can scale back to estimate the response to a much smaller SST anomaly.

## 3. GCM responses

Two 2000-day integrations, after throwing away the spinup period, have been conducted with the idealized GCM for the warm and cold SST anomalies shown in Figs. 2a and b, respectively. We average over the 2000-day integration to get the stationary responses. Figures 2c–f are the zonally asymmetric precipitation and evaporation in the positive and negative anomaly cases. There is a positive (negative) rainfall anomaly at approximately the same latitude as the positive (negative) SST anomaly. The precipitation anomaly is extended northeastward from the SST's. The maximum anomalous precipitation is 0.18 cm day$^{-1}$ in the positive case and only 0.06 cm day$^{-1}$ in the negative case. One notices the strong nonlinearity in the amplitude of the rainfall anomaly. The evaporation anomaly is shifted slightly westward from the SSTs. A similar nonlinear relation is seen in the amplitude of the evaporations. One possible explanation for that is the Clausius–Claperon equation, which indicates that the saturation vapor pressure, and thus the evaporation, is a highly nonlinear (exponential) function of the temperature. It is clear from Fig. 2 that precipitation and evaporation is the main balance in the moisture budget equation; thus one sees the similar nonlinear behavior in precipitation. In both positive and negative cases, the anomalous precipitation is weaker than the anomalous evaporation and is shifted northeastward. The cause of this shift will be discussed more in the moisture budget calculation in section 5.

The magnitude of the anomalous precipitation in

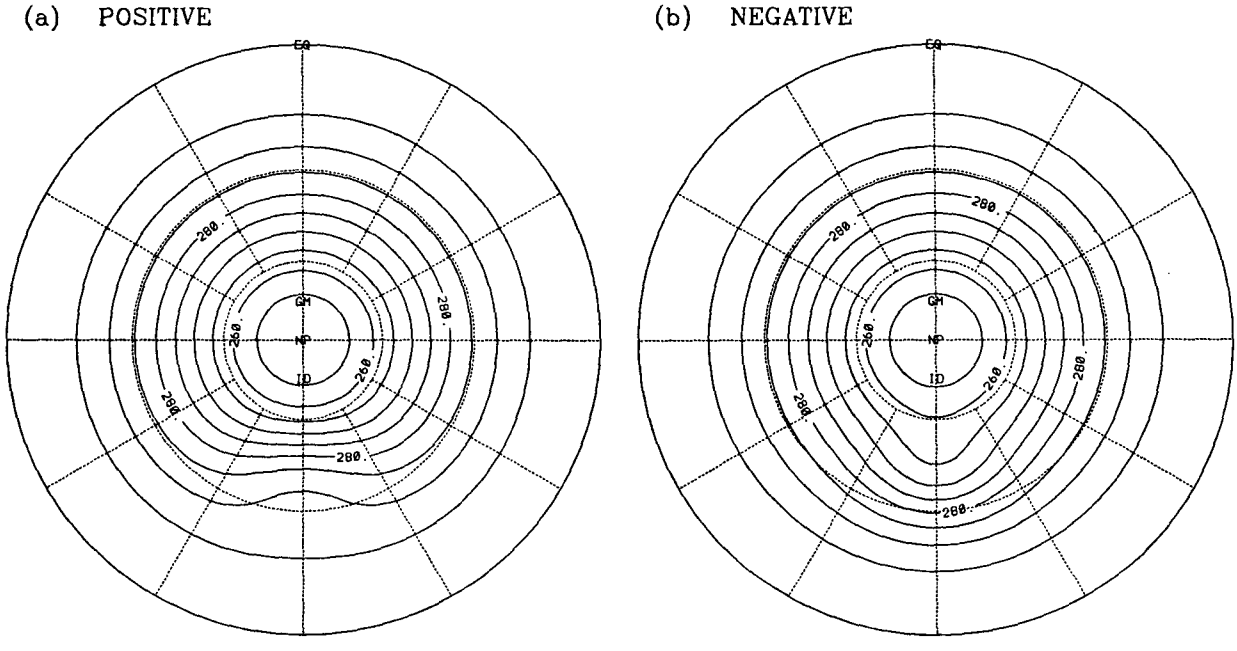


FIG. 1. Total SST distribution in the midlatitude positive (a) and negative (b) anomaly cases in Northern Hemisphere. Contour interval is 5 K. Lines of latitude and longitude are drawn every 30°.

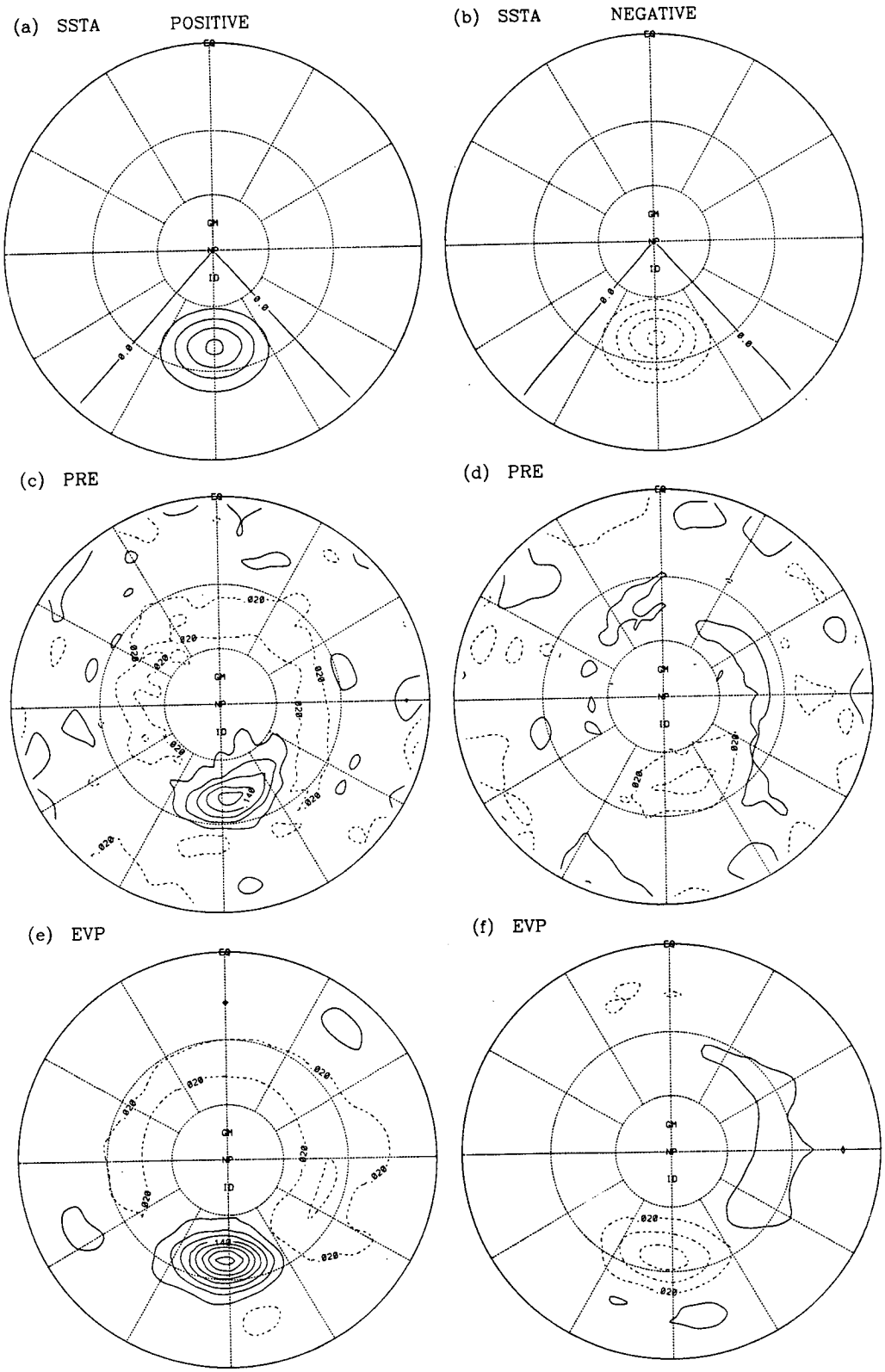


FIG. 2. Zonally asymmetric SST distribution in the positive (a) and negative (b) anomaly cases with contour interval 2 K; zonally asymmetric precipitation in the positive (c) and negative (d) cases with contour interval 0.04 cm day$^{-1}$; zonally asymmetric evaporation in the positive (e) and negative (f) cases with contour interval 0.04 cm day$^{-1}$. Positive contours are solid and negative ones are dashed; zero contours in (c)–(f) are omitted.

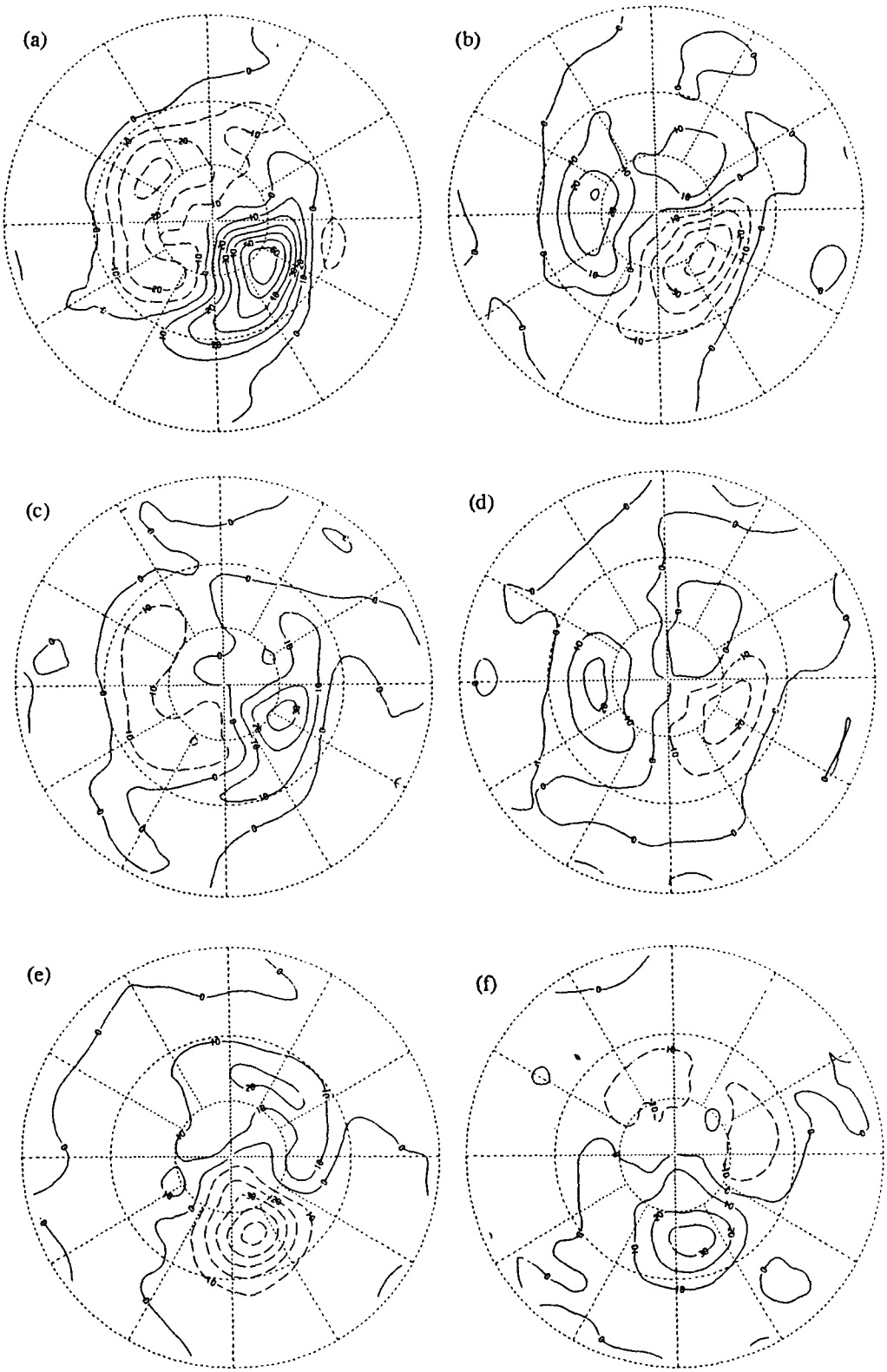


FIG. 3. Eddy geopotential height at 205 mb (a and b), 515 mb (c and d), and 990 mb (e and f) in positive and negative anomaly experiments, respectively. Contour interval is 10 gpm; positive contours are solid and negative ones are dashed.

the positive case is comparable to the climatological rainfall at these latitudes (about 0.3 cm day$^{-1}$). Even in the negative anomaly case, the rainfall suppression is nearly 0.1 cm day$^{-1}$, which is still a significant perturbation at these latitudes. Obviously, most of the rainfall anomalies in Figs. 2c and 2d are directly forced by the SST anomaly. The relation between the rainfall anomaly and the midlatitude SST anomaly in other more realistic GCM experiments is not as straightforward as in this idealized case. In LN, for example, the in situ anomalous precipitation is negative when the SST anomaly is positive off the Newfoundland coast, and there are weak increases in precipitation north of the warm anomaly. The mechanism that controls the precipitation anomaly must be quite different in the two cases.

The eddy geopotential height anomalies at three different pressure levels are shown in Fig. 3 for both positive and negative anomaly experiments. The dominant features in the upper troposphere consist of a high (low) about 45° downstream of the warm (cold) SST anomaly and a weaker compensating low (high) upstream, nearly a wavenumber one response. At 515 mb, the anomaly pattern remains the same but with half of the amplitude, and the whole pattern is shifted about 15° downstream. At the surface level, however, the anomaly is dominated by a strong low (high) center located slightly downstream and northward of the warm (cold) SST anomaly, with comparable amplitude to the downstream high (low) in the upper troposphere.

The vertical-longitude distribution of the geopotential height anomaly at 50°N is shown in Figs. 4a and b for positive and negative cases, respectively. One finds an abrupt phase reversal at around 515 mb (680 mb) for positive (negative) anomaly cases. The surface response decreases rapidly upward, while the upper tropospheric response increases upward and, at the same time, tilts westward. As discussed later, one should not think of the lower and upper tropospheric responses as part of the same vertically propagating wave.

The strong baroclinic responses in the idealized GCM contrast sharply to those in LN, who find an equivalent barotropic structure of the extratropical response. This equivalent barotropic structure is also found by other GCM simulations (Pitcher et al. 1987; Palmer and Sun 1985) as well as in the observation (Wallace and Jiang 1987; Wallace et al. 1990). On the other hand, Fig. 4a compares very favorably to Fig. 5 of Hoskins and Karoly (1981), which shows the linear model response to a shallow, circular heat source centered at 45°N with the Northern Hemisphere winter flow as the basic state. It is also worth noting that the

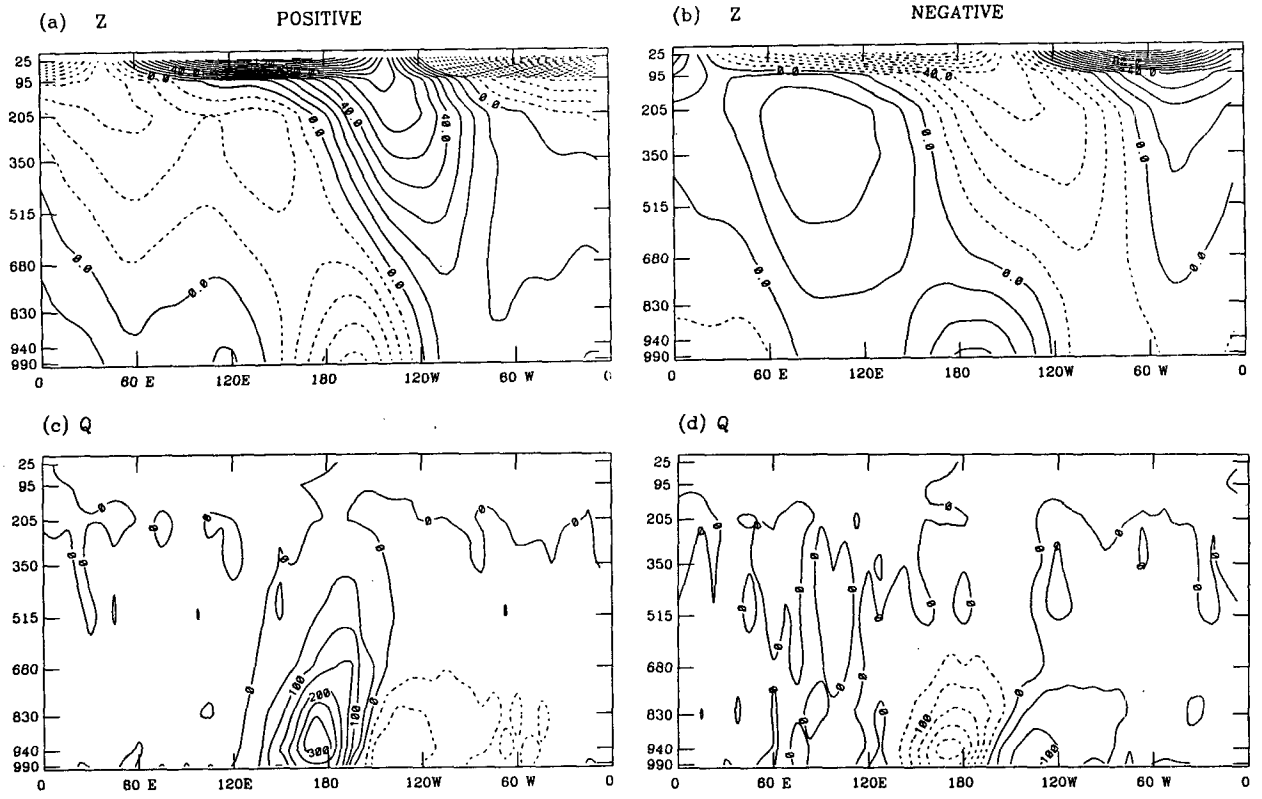


FIG. 4. Vertical-longitude cross sections of eddy geopotential height at 50°N (a,b) and diabatic heating at 40°N (c,d) in positive and negative anomaly experiments. Contour intervals are 10 gpm for (a) and (b) and $5 \times 10^{-6}$ K s$^{-1}$ for (c) and (d); negative values are dashed.

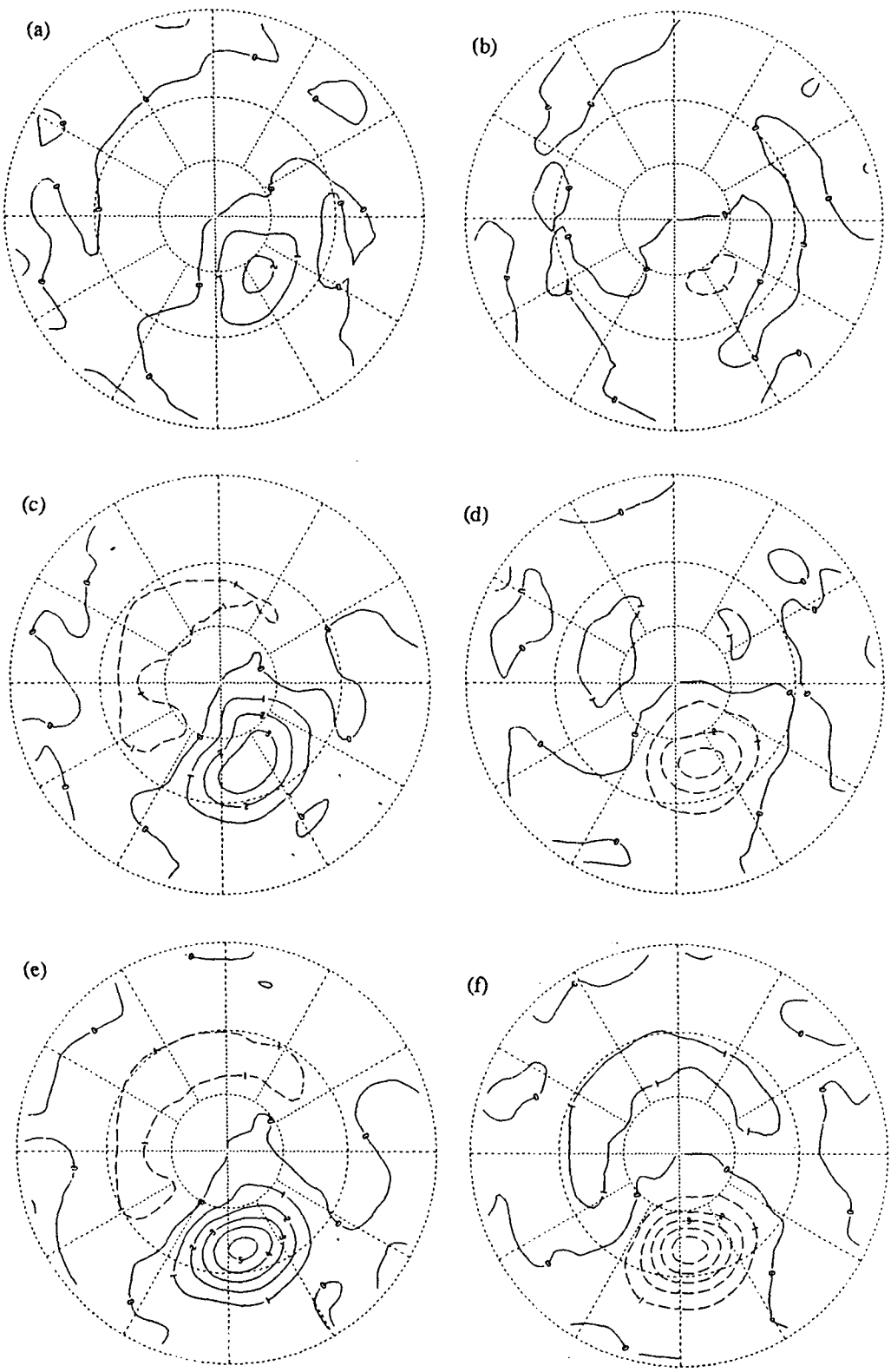


FIG. 5. Eddy temperature at 515 mb (a and b), 830 mb (c and d), and 990 mb (e and f) in positive and negative anomaly cases, respectively. Contour interval is 1 K; positive contours are solid and negative ones are dashed.

amplitude of the stationary wave response of the idealized GCM to the prescribed SST anomaly (less than 100 m per 10 K at the 205 mb level) is considerably lower than both the observation and results based on more realistic models. These discrepancies suggest that the nature of the atmospheric response to a midlatitude SST anomaly in a zonally symmetric control climate differs significantly from that in a more realistic, zonally asymmetric control climate.

The simple vertical structure of the responses in the idealized GCM can be understood by the following scaling arguments suggested by Held (1983). If the diabatic heating is very shallow in the vertical (which is true in this case), one can neglect the adiabatic cooling term in the thermodynamic equation within the heated region. A particular solution can then be obtained by integrating the heating downward, so that this local response has the same shallow vertical structure as the heating. The diabatic heating is balanced by advecting cold air from the polar region, thus a trough is forced to the east of the heating. One expects downward motion at the center of the heating, so that the associated vortex compression balances the creation of vorticity due to the southward motion. A homogeneous solution is then forced by an "equivalent mountain," which balances this downward motion to satisfy the lower boundary condition (the total vertical motion at the surface must be zero). The "equivalent mountain" has upward slope right at the heating center, thus forming a ridge about a quarter wavelength downstream of the heating. An anticyclone is then forced close to the "mountain" ridge. For long wavelengths, this wave propagates in the vertical and slopes westward with height just as seen in Fig. 4a.

It is interesting to note that the cooling (Fig. 4d) associated with the negative SST anomaly is shallower than the heating (Fig. 4c). This difference in vertical structure between positive and negative cases is also reflected in the geopotential height responses (Fig. 4a,b). Another feature one notices in Figs. 3 and 4 is that the geopotential height responses are somewhat more linear with respect to the SST anomaly than the heating anomaly itself. The precipitation anomaly in the positive case is about three times as strong as in the negative case; however, the geopotential height response in the positive case is only one and one-half times as strong as in the negative case. This surprising difference can be explained by the different vertical heating distributions. Although the heating in Fig. 4c penetrates deeper into the upper troposphere than the cooling, the maximum amplitude of the heating at 940 mb is similar between the two cases ($3 \times 10^{-5}$ vs. $2.5 \times 10^{-5}$). From Eq. (6.32) in Held (1983), a particular solution is the vertical integral of diabatic heating weighted by the inverse of zonal mean zonal flow. Thus the contribution of the heating higher up to this particular solution is weaker than the heating lower down, due to the fact that zonal mean zonal flow increases upward. This explains that the difference between the particular solution in positive and negative cases is smaller than the difference between the vertically integrated heating (precipitation). The homogeneous solution shows the same tendency as the particular solution since it is the response to the "equivalent mountain."

The temperature anomalies shown in Fig. 5 show warming and cooling throughout the entire troposphere for positive and negative anomaly cases, respectively. In the interior of the atmosphere, the warming and cooling are relatively weak. They reach their maximum values at the lowest level, about half of the SST anomaly. The eastward tilt of the temperature anomaly with height within the troposphere seen in Fig. 5 can be explained by waves that are propagating in the vertical, a westward tilt in the height perturbation for a vertically propagating wave results in an eastward tilt in the temperature perturbation. The temperature perturbation forced by the midlatitude SST anomaly is again consistent with the shallow heating result of Hoskins and Karoly (1981). They show from the thermal wind relation that, in contrast to a deep heating that gives negative temperature perturbation downstream, shallow heating will force a positive vorticity perturbation decreasing with height and therefore a positive temperature perturbation.

## 4. Linear model diagnosis

The steady, $\sigma$-coordinate, 9-level spectral model, linearized about a zonally symmetric basic state described in TH is used to study these GCM responses. The zonal mean basic state is taken from the zonally averaged flow of the corresponding anomaly experiments. The forcing includes diabatic heating and the tendency due to transients. The transient tendencies are calculated as the residual of the full GCM equations when the GCM time mean flow is substituted into these equations. Biharmonic diffusion with coefficient $1 \times 10^{17}$ m$^4$ s$^{-1}$ and boundary Rayleigh friction with time scale 1 day at the surface, decaying linearly to zero at $\sigma = 0.8$, are utilized in the linear model calculation in this study. Unless otherwise indicated, there are no other dissipative processes in the model.

### *a. Total GCM forcing*

When the linear model is forced by total GCM forcing, i.e., heating plus transients, the responses are shown in Fig. 6 for the geopotential height anomaly in the same format as Fig. 3. The linear model gives excellent simulations of the idealized GCM as can be seen by comparing Fig. 6 with Fig. 3. All the anomalies, including the downstream high (low) in the upper troposphere and the surface low (high) for the positive (negative) anomaly case, are very well captured by the linear model. Both the shape and amplitude of the

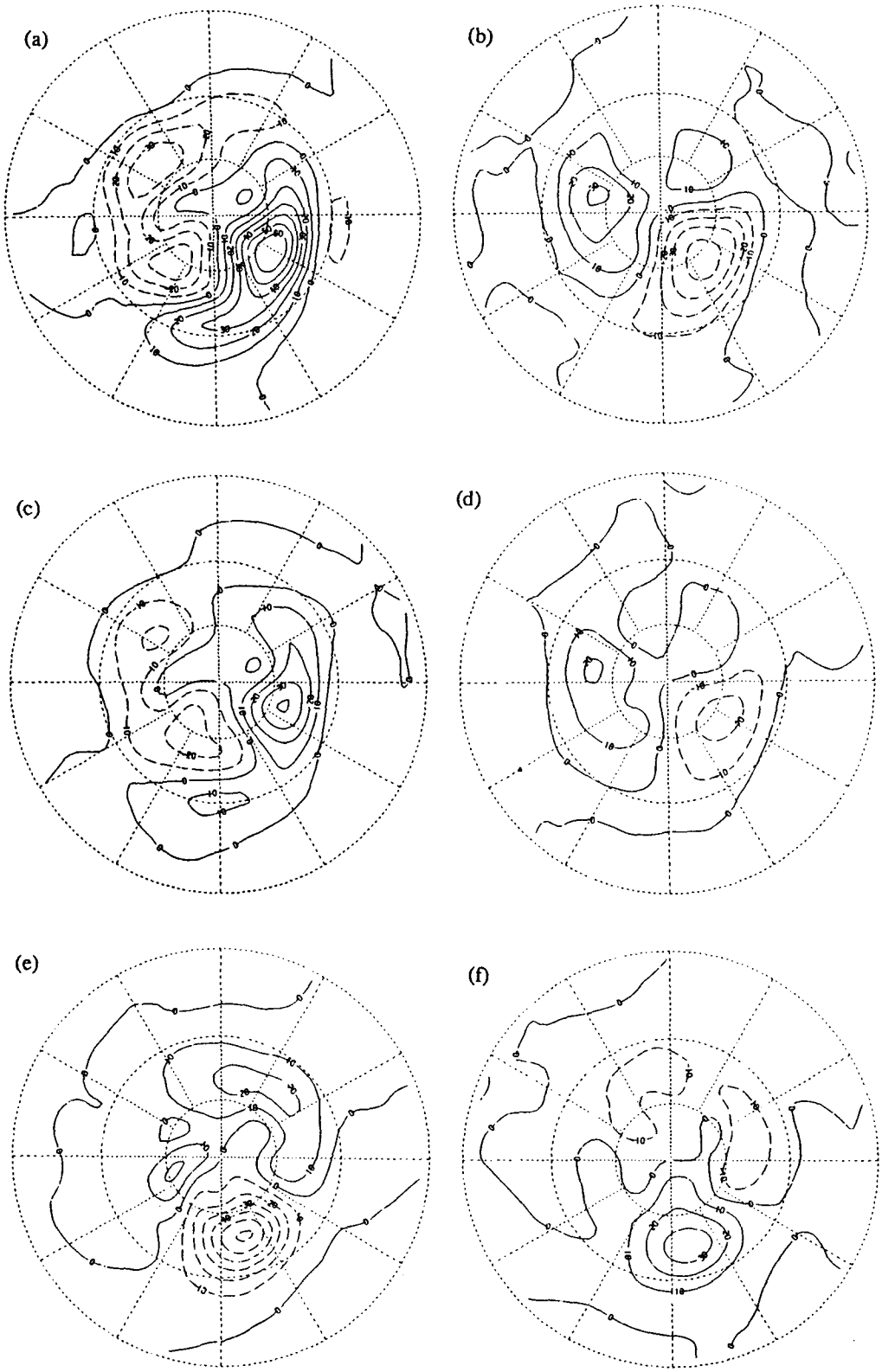


FIG. 6. Same as Fig. 3, but obtained from the linear model when it is forced by diabatic heating plus transients.

anomalies are accurately reproduced in Fig. 6. The temperature response and the vertical structure of the response (not shown) resemble those shown in Figs. 4 and 5 for the GCM as well. The only exception is the surface temperature perturbation, which is a bit noisy in comparison to the corresponding GCM pattern. The noisiness is presumably due to the complex structure of the diabatic heating at the lowest model level. The surprisingly good simulation by the linear model suggests that the atmospheric response to a midlatitude SST anomaly is quite linear in the idealized GCM, at least when we think of the forcing by transients as imposed. This is one of the advantages of using the idealized GCM instead of a more realistic one. We now examine the forcing by transients more closely.

### b. *Thermal transients parameterization*

We first separate the GCM thermal forcing into diabatic heating and transient heat flux convergence and force the linear model with these two parts separately. The eddy geopotential height at 205 mb, forced by diabatic heating in isolation and by thermal transients in isolation, are shown in Fig. 7a–d for both positive and negative anomaly experiments. One notices that the eddy geopotential in the upper troposphere in Figs. 7a and 7b shows more small scale features compared with the same response to total forcing (Figs. 6a and 6b), especially in the meridional direction. The downstream high centered at 120°W in Fig. 6a for the positive anomaly case is now split into two centers, one upstream and one downstream. The upstream one in Fig. 7a is shifted southward about 20° and its amplitude is reduced. In the negative anomaly case, the downstream low in Fig. 6b has been similarly shifted southeastward in Fig. 7b and greatly reduced. The geopotential height anomaly forced by thermal transients in Figs. 7c and d also shows a somewhat noisy picture. However, one finds a significant high (low) in Fig. 7c (7d). Obviously, thermal transient forcing in this case is just as significant as the diabatic heating itself. There is some cancellation between the heating-forced and the thermal transient-forced anomalies in Fig. 7 in the polar region. In the subtropics and downstream of the forcing, however, the heating and thermal transients are constructive.

Figures 7e and f give the sum of heating-forced (Figs. 7a and 7b) and the thermal transient-forced anomaly (Figs. 7c and 7d) for positive and negative anomaly cases, respectively. The eddy geopotential height in Figs. 7e and f compares much better to the GCM responses. Upon close inspection, the downstream high in Fig. 7e is slightly weaker than the corresponding one in Fig. 6a, and it is shifted a little southwestward. The far upstream low is too far to the west. One can still see some of the small scale structures in Figs. 7e and f. The differences between Fig. 7f and Fig. 6b for the cold anomaly case are somewhat bigger, though Fig. 7f still gives a much better comparison with the response to total forcing than the heating itself. These moderate differences are due to the momentum transient forcing that we will discuss in more detail in the next subsection.

The difficulty of getting a smoother anomaly pattern from the heating in isolation is solved when one appropriately parameterizes the damping effect of the low-level transient heat flux convergence. The detailed structure of the temperature tendency due to thermal transients at level 8 ($\sigma = 0.94$) is shown in Fig. 8a for the positive anomaly case. The transients tends to reduce the temperature anomaly at the center of the anomaly and increase it away from the center, acting very much like horizontal diffusion. The Laplacian of the temperature anomaly is shown for the same level in Fig. 8b. The horizontal distributions in Figs. 8a and b are surprisingly similar, which indicates that a simple parameterization of transient heat flux convergence as a uniform horizontal temperature diffusion can mimic the GCM's behavior quite accurately. The particular level we choose to show here is very typical of other vertical levels, except that the thermal transient forcing is very weak above 515 mb.

This parameterization is then utilized in the linear model, with a horizontal thermal diffusion coefficient of $2 \times 10^6$ m$^2$ s$^{-1}$. The linear model responses to diabatic heating and momentum transients, with biharmonic diffusion and boundary Rayleigh friction plus the *horizontal thermal diffusion*, are shown in the top panel of Fig. 9 for the geopotential height anomaly at 205 and 990 mb in the positive anomaly case. (For brevity, the results will only be shown for the positive anomaly case from now on; the negative anomaly case shares most of the same features.) Figure 9a is very similar to the corresponding anomalies in Fig. 6a. One finds a similar high about 60° downstream and north of the SST anomaly and low geopotential height upstream. Some differences between Fig. 6a and Fig. 9a are that the amplitudes of the downstream high and the immediate upstream low center are reduced about 15% in Fig. 9a, and the anomaly does not extend as far to the north.

At the surface, the linear model with thermal diffusion again captures the dominant structure at this level: a strong low center slightly downstream and north of the warm SST anomaly. However, a careful comparison reveals that the shape of the anomaly in Fig. 9b extends more towards the southeast and the amplitude intensifies somewhat. The differences between the linear model response to heating plus momentum transients with thermal diffusion (Fig. 9a,b) and the linear model response to total forcing without thermal diffusion (Fig. 6a,e) are due to the fact that GCM's thermal transients are not precisely identical to a uniform horizontal diffusion. Varying the horizontal thermal diffusion coefficient, we find the linear model response can not be improved further. Mimicking the horizontal structure of the thermal transients by allow-

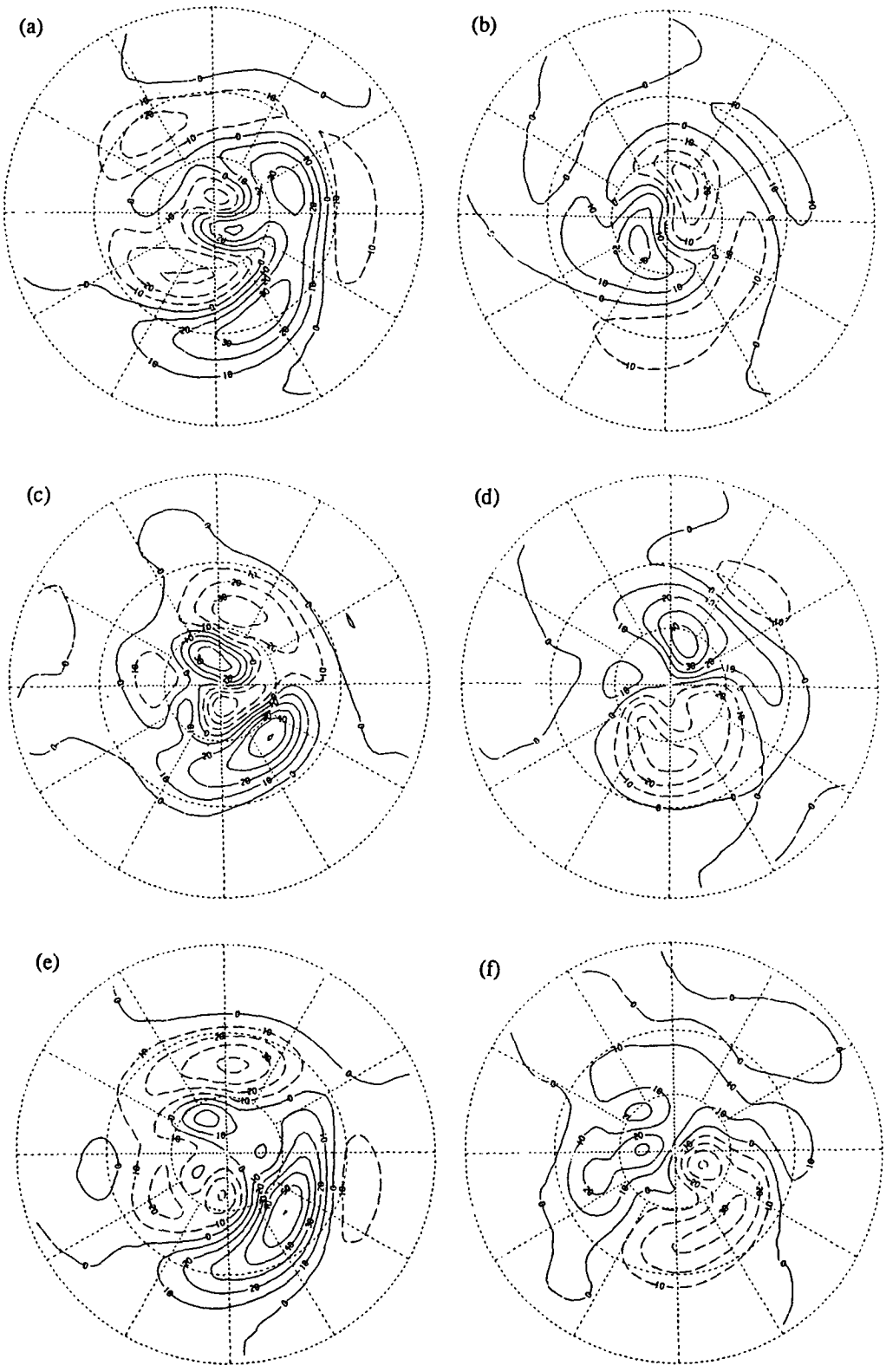


FIG. 7. Linear model eddy geopotential height at 205 mb forced by (a) positive anomaly diabatic heating, (b) negative anomaly diabatic heating, (c) positive anomaly thermal transients, (d) negative anomaly thermal transients, (e) positive anomaly diabatic heating plus thermal transients, and (f) negative diabatic heating plus thermal transients. Contour interval is 10 gpm; positive contours are solid and negative ones are dashed.

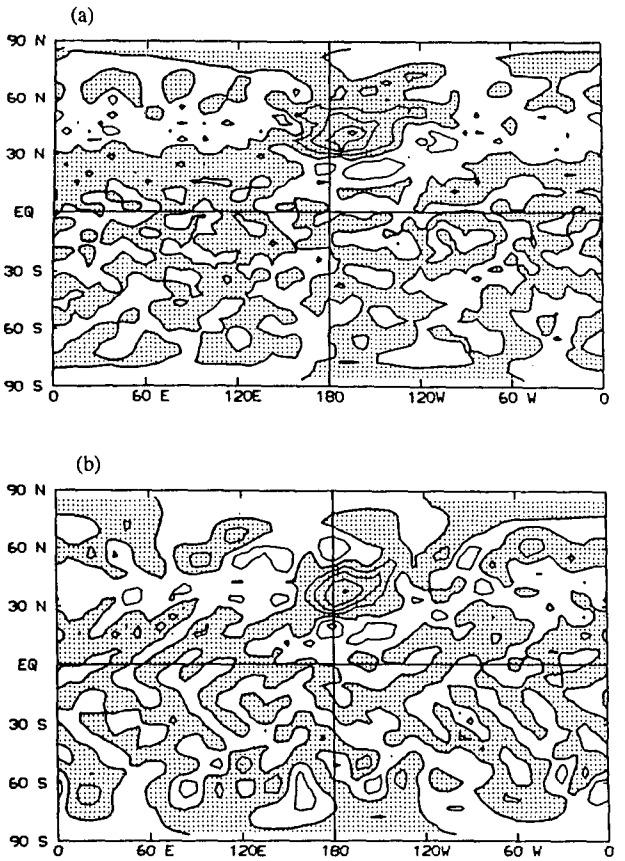


FIG. 8. (a) Temperature tendency due to transient heat flux convergence in positive anomaly case at level 8 ($\sigma = 0.94$) with contour interval $5 \times 10^{-6}$ K s$^{-1}$; (b) Laplacian of eddy temperature in positive anomaly case at the same level with contour interval of $1 \times 10^{-12}$ K m$^{-2}$. Negative values are shaded.

ing latitudinal dependence in the diffusion coefficient might allow one to improve the simulation, but this introduces too much arbitrariness.

### c. *Diabatic heating versus momentum transients*

The separation of the linear model response into parts forced by diabatic heating and by momentum transients, when thermal transients are parameterized by a horizontal temperature diffusion, is shown in Figs. 9c–f for upper and lower tropospheric eddy geopotential height. The upper tropospheric response to diabatic heating in isolation is again dominated by a downstream high and a broad upstream low. At the surface, there is a strong low center slightly downstream of the SST anomaly. To first approximation, we find the linear model response to diabatic heating in isolation gives a good simulation of the GCM anomaly. This result explains the similarity of the GCM response and the linear model response to a midlatitude shallow heat source in Hoskins and Karoly (1981), in which thermal transients are represented by a 10-day low-level thermal damping.

There are still significant differences between the GCM anomaly and the response to diabatic heating in isolation. The amplitude of the downstream high in Fig. 9c is reduced another 15% from the response to both heating and momentum transients (Fig. 9a), and the center has been shifted some 20° westward and somewhat southward. Significant differences are also found at around 50°N, 45°E, where a closed low center with amplitude of 44 gpm in Fig. 9a almost completely disappears, leaving only a broad band of negative anomaly in Fig. 9c. These two major differences between Figs. 9a and c are explained by the effect of momentum transients. There are two major centers in the linear model upper tropospheric response to momentum transients (Fig. 9e); one is the high at 120°W, which causes the shift of the downstream high northeastward from Fig. 9c to a, and another is a low center at around 45°E, which produces the low at that location in Fig. 9a. At the surface, the influence of momentum transients is relatively small. However, one notices that the vertical structure of the momentum transient-forced anomaly is equivalent barotropically. The dominant baroclinic structure of the GCM anomaly is entirely due to the diabatic heating in this model.

The different vertical structures forced by diabatic heating and anomalous transients in Figs. 9c,d and e,f suggest that the equivalent barotropic wavetrain found in realistic GCM experiments (e.g., Palmer and Sun 1985; Pitcher et al. 1987; Lau and Nath 1990) is mainly forced by momentum transients, due to the interaction between the storm track eddies and the anomalous wavetrain forced by the SST anomaly. This interaction is clearly not as significant in an idealized GCM in which the control climate is zonally symmetric. The lack of strong momentum transient forcing also explains the weakness of the response to midlatitude SST anomaly in the idealized GCM. Diabatic heating directly associated with the SST anomaly, as the dominant forcing in the idealized case, can only force a rather moderate amplitude in geopotential height responses. However, the strong anomalous momentum transient flux convergence associated with the shift of storm track axes, as discussed in LN, is able to force a much stronger climate anomaly.

### d. *Discussion*

The predominance of the diabatic heating effect in the idealized GCM contrasts sharply to the realistic GCM results in LN, which shows the dominance of the shift of storm track axis and associated forcing by anomalous transient eddy momentum fluxes. As we have seen in Fig. 1, the strong SST anomaly we specified in the anomaly experiments shifts the maximum meridional gradient of the SST significantly. Even the atmospheric temperature perturbation at 515 mb still gives an anomaly of about 2 K (Fig. 5a), which is much weaker than the SST anomaly specified at the

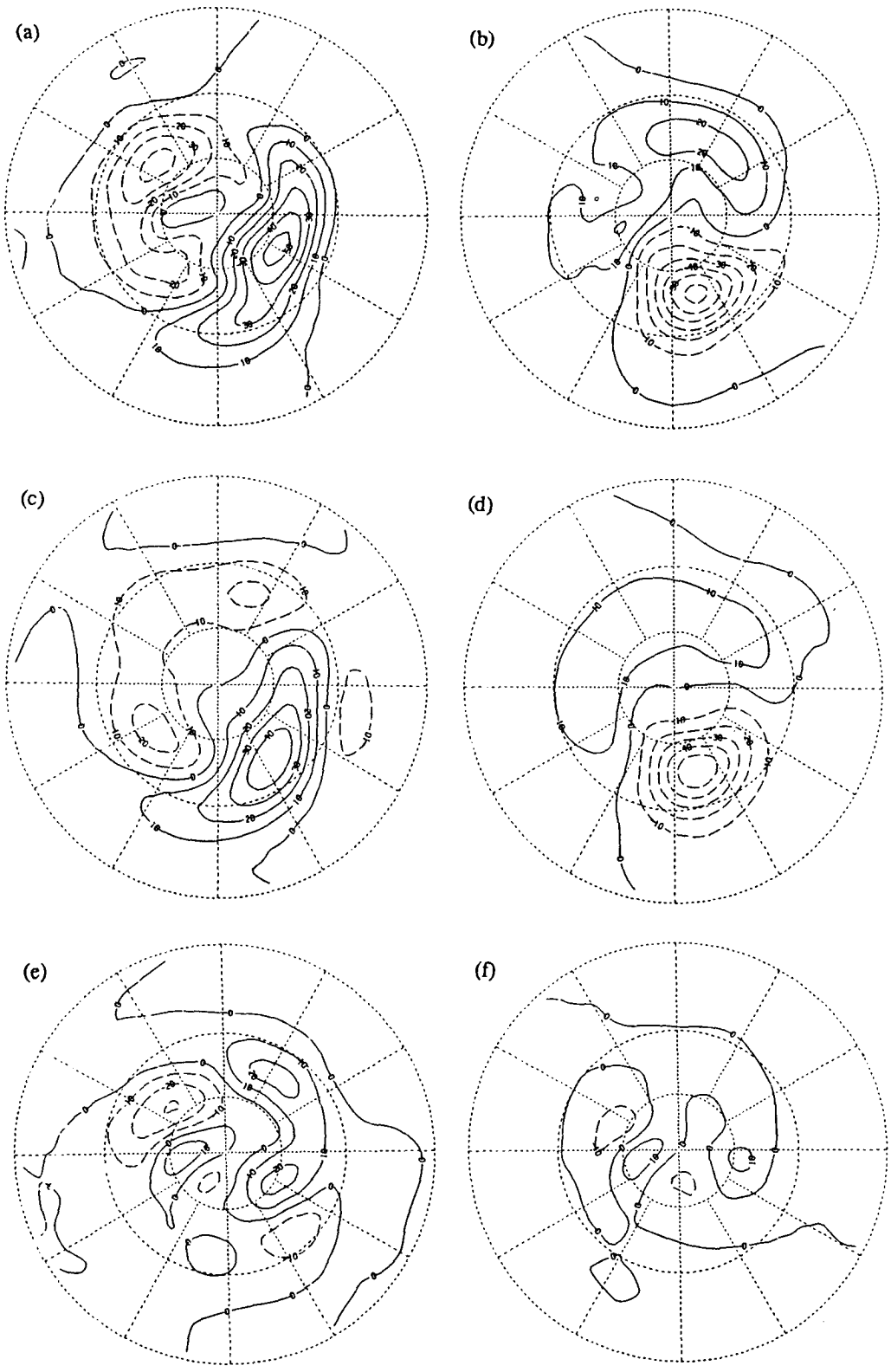


FIG. 9. Linear model (with thermal diffusion) eddy geopotential height at 205 mb and 990 mb forced by diabatic heating plus momentum transients (a and b), diabatic heating only (c and d), and momentum transients only (e and f) in positive anomaly case. Contour interval is 10 gpm; positive contours are solid and negative ones are dashed.

surface in the idealized GCM, but it would not be a small perturbation in the real atmosphere. One then expects to see a strong influence of this change of baroclinicity in the lower troposphere on the transient eddies, particularly the eddy transient momentum flux convergence. Although some changes do occur (we hope to discuss these in future work), they have little effect on the mean response. On the other hand, the observed ocean surface temperature anomaly in the real atmosphere is relatively weak, and the change in baroclinicity in the lower troposphere should be less significant. However, the GCM results suggest the opposite: a small SST perturbation in a realistic GCM can cause a significant change in midlatitude baroclinic wave momentum flux convergence, yet a large SST perturbation in an idealized GCM with zonally symmetric control climate does not create a significant enough change in the upper tropospheric wave fluxes to modify the mean flow substantially.

From the nonlinear baroclinic wave life cycle studies such as Simmons and Hoskins (1978), large poleward momentum flux occurs after cessation of linear growth, associated with the Rossby wave radiation towards the tropics. As shown by Blackmon et al. (1977) and Lau (1979), Northern Hemisphere (NH) synoptic-scale transients are organized into well-defined storm tracks that are located downstream and poleward of the mean jet maxima. A three-dimensional extension of the baroclinic wave life cycle is suggested by Hoskins (1983): wave activity is generated by baroclinic instability at low levels off the east coasts of the NH continents, it then propagates downstream and vertically to upper-tropospheric levels, and then propagates equatorward into regions where the wave activity is dissipated. Based on this three-dimensional picture, there are two possible ways to change the momentum fluxes. The first is to change the baroclinic instability at low levels by changing the atmospheric thermal structure, and the second is to perturb the upper tropospheric flow downstream in the barotropic decay region. Due to the lack of climatological zonal-asymmetries, there is no well-defined baroclinic growth and barotropic decay regions in the idealized GCM. Perhaps this is why both mechanisms are inefficient in this model. Realistic GCM calculation suggests that the second mechanism in particular can be very significant, but only if the momentum fluxes are strongly localized. This picture seems consistent with the tropical SST anomaly results discussed in Ting and Held.

As suggested by Palmer and Sun (1985), the shallow nature of the midlatitude heating forced by the SST anomaly may be modified by the vertical heat fluxes. This modified vertical heating distribution might contribute to the equivalent barotropic response as well. We find here that both the vertical structure of the heating and the temperature tendency due to thermal transients are very shallow. Thermal transients modify the horizontal structure of the heating, but do not deepen it substantially. The sum of heating and thermal transients gives a similar shallow vertical structure, which suggests that the direct modification of the vertical structure of the heating by the transient eddy vertical heat fluxes is not significant. The eddies may still have a more indirect effect on the vertical structure of the latent heating by modifying the environment in which the model's convection occurs.

## 5. Moisture budget and air–sea interaction

We have shown in the last section that a linear model can simulate the GCM's anomalous response to a midlatitude SST anomaly very well, given the GCM's three-dimensional heating field and transient eddy fluxes. With a simple horizontal diffusion included in the linear model to replace the thermal transients, one can even get a good picture of the GCM's response with the heating field as the only forcing, totally ignoring the momentum transients. The idealized GCM experiments then provide a good place to study the relation between the anomalous diabatic heating and the ocean surface temperature anomaly. Many simple modeling studies relate the sensible and latent heat release to the air–sea temperature difference and assume an arbitrary vertical heating profile (Frankignoul 1985, for example). Due to the lack of observations of the heating, it is very difficult to determine whether it is meaningful to compare the atmospheric response to these heating distributions with observed atmospheric anomalies.

### *a. Sensible heating parameterization*

The total diabatic heating taken from the GCM includes the radiative, sensible, and convective heat flux convergences. The anomalous radiative heat flux caused by the SST anomaly is relatively weak. (The radiative effects would certainly be larger in a model in which clouds were predicted, rather than prescribed.) The vertically integrated sensible and latent heat are comparable in magnitude, about 0.5 K day$^{-1}$ each. However, the separation of sensible and latent heating effects in the linear model is difficult due to the strong negative convective heating at the lowest model level as a result of convective adjustment. This strong negative heating is balanced by the positive sensible heat flux at this same level. The linear model response to sensible or latent heating in isolation gives a rather noisy structure due to this strong cancellation. Instead, we try to parameterize the sensible heat flux over the ocean surface by a boundary Newtonian damping, which damps the lowest three level temperature back to the ocean surface temperature at the same rate as Rayleigh friction. This sensible heating parameterization is possible because the surface temperature is prescribed everywhere in the idealized GCM; this would be much more difficult in a model with a land surface.

Figure 10 contains the linear model response to la-

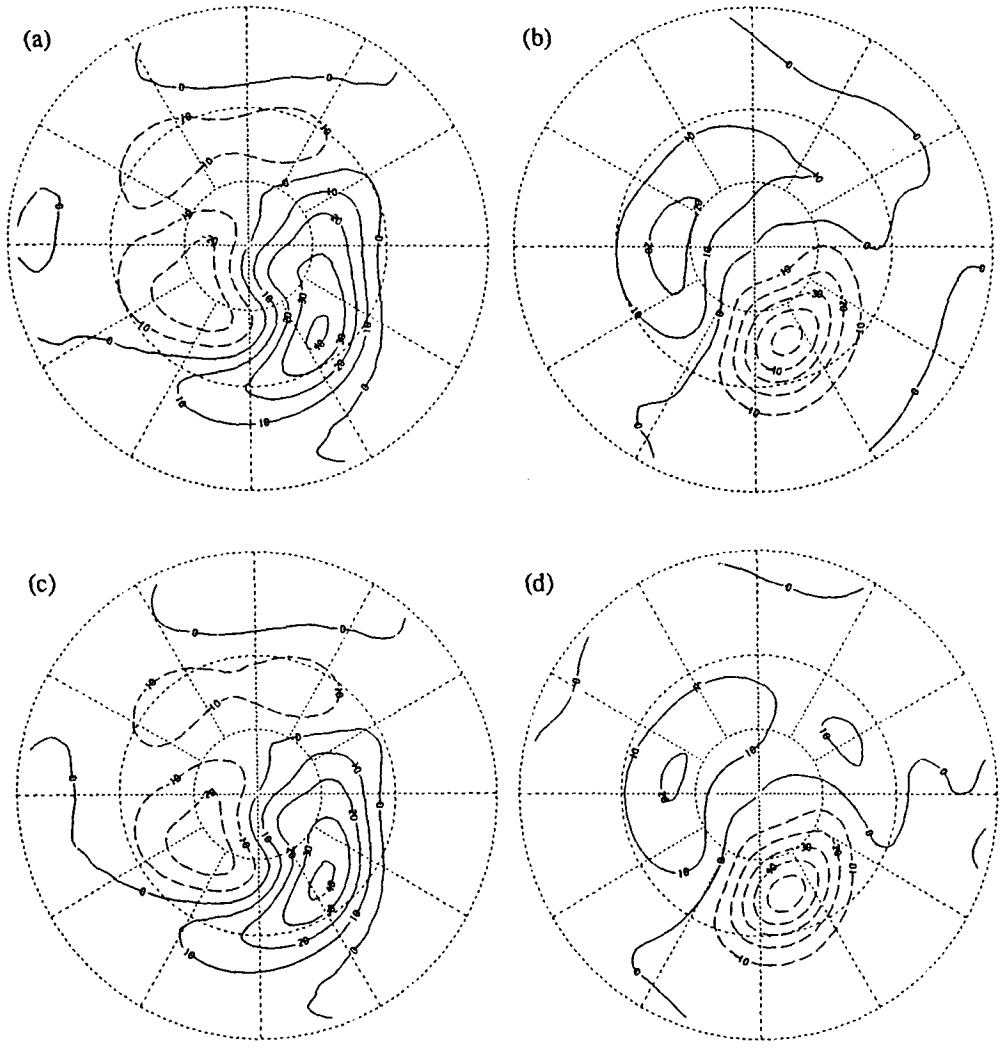


FIG. 10. Linear model (with thermal diffusion) eddy geopotential height at 205 mb and 990 mb forced by sensible plus convective heating (a and b) and convective heating plus Newtonian damping (c and d) (details in the text). Contour interval is 10 gpm; positive contours are solid and negative ones are dashed.

tent heating plus sensible heating (a and b) and to latent heating plus Newtonian damping (c and d) for the geopotential height anomaly at 205 mb and 990 mb levels. The linear model results for the two cases are very similar, which suggests that the sensible heating parameterization is quite accurate. Both cases show a somewhat reduced amplitude in the upper troposphere compared with the response to total diabatic heating in Fig. 9c, which is due to the small contribution of radiative heat flux. The surface lows are very similar with or without radiative heating.

The relative importance of the sensible heating and latent heating is examined in Fig. 11. Shown are the geopotential height anomaly at 205, 515, 990 mb levels forced by sensible heating when it is parameterized as Newtonian cooling (on left), and the anomalies forced by latent heating only (on right). The latter are obtained by subtracting the left-hand panels from the total response to latent heating with Newtonian damping. The contour interval for the geopotential height anomaly in Fig. 11 is half of that in Fig. 10. In the upper troposphere, the geopotential height anomaly is mainly forced by latent heating. The maximum anomaly in Fig. 11a is slightly less than 10 gpm, while it is more than 30 gpm in Fig. 11b for the latent heating-forced anomaly. The phases of the anomaly forced by sensible heating and that forced by latent heating are approximately equal. At the 515 mb level, the difference in amplitude between sensible heating-forced and latent heating-forced height anomalies is smaller than at upper troposphere. The amplitude of the anomaly forced by sensible heating (Fig. 11c) is now half of that forced by latent heating (Fig. 11d). At the surface, sensible and latent heating force similar lows downstream

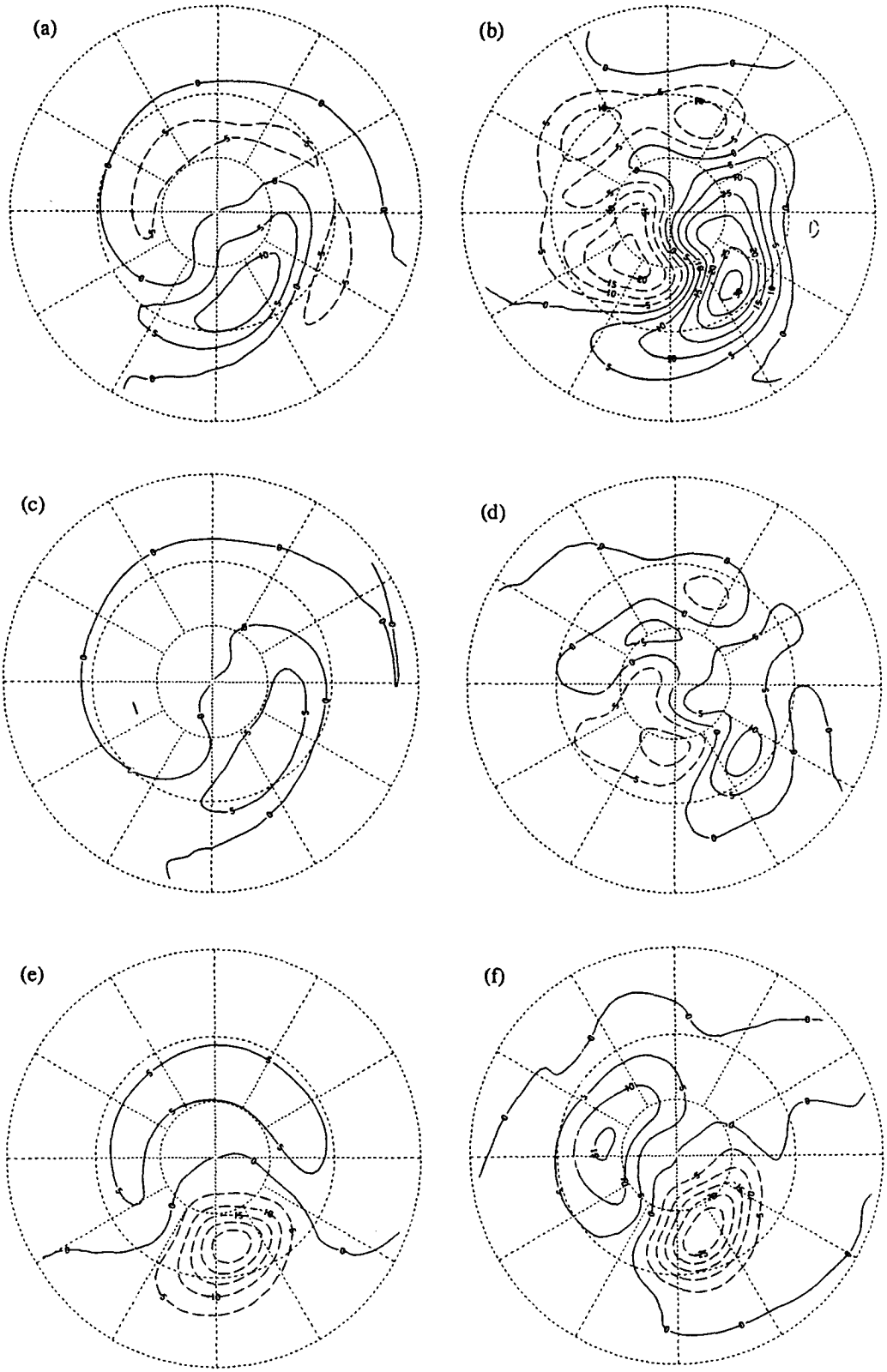


FIG. 11. Linear model (with thermal diffusion) eddy geopotential height at 205, 515, and 990 mb forced by sensible heating effect when it is parameterized as boundary Newtonian form (a, c, and e) and convective heating in isolation (b, d, and f). Contour interval is 5 gpm; positive contours are solid and negative ones are dashed.

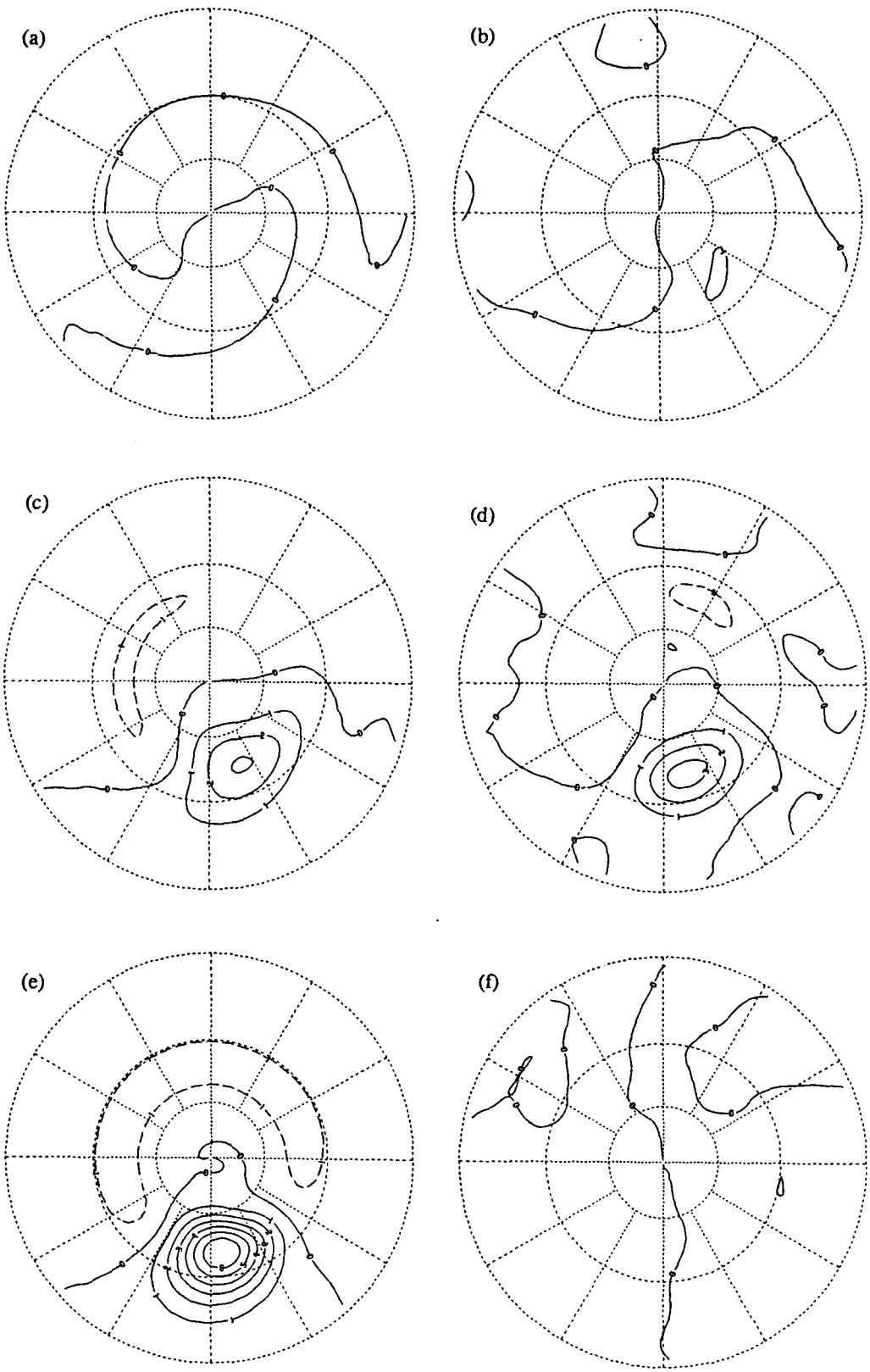


FIG. 12. Same as Fig. 11, but for eddy temperature at the 515, 830, and 990 mb levels.

of the heat source, and the amplitude forced by sensible heating is about the same as that forced by latent heating.

The temperature anomalies at 515, 830, and 990 mb are shown in Fig. 12. In the interior of the atmosphere, the temperature anomalies are dominated by that forced by latent heating. At the top of boundary layer (830 mb), the eddy temperature forced by latent heating is about the same magnitude as that forced by sensible heating. However, when one goes down to the shallow boundary layer (940 and 990 mb), one finds that the eddy temperatures are totally determined by the SST anomaly through the sensible heat fluxes, and they are also very similar to their GCM counterparts (compare Fig. 5e with Fig. 12e). The temperature anomaly forced by latent heating is negligible at both 940 and 990 mb levels.

Nigam and Lindzen (1988) have proposed a simple relation between SST and the surface pressure distribution in the tropics. They find boundary layer temperatures are strongly tied to SST by turbulent vertical mixing. These horizontal temperature variations can force horizontal pressure gradients, which can then force boundary flow of about the observed magnitude in the tropics. The results in Fig. 12 confirms that boundary temperature is totally determined by SST through sensible heat fluxes in the midlatitudes of the GCM as well. However, the boundary flow is still partly forced by latent heat release in our experiment. We caution that the relative importance of sensible and latent heating could be sensitive to the boundary layer parameterization.

The vertical integral of the latent heating is equal to the precipitation. If the vertical heating profile could be assumed to be similar at all horizontal grid points, then one could write,

$$\dot{Q}'(\lambda, \theta, \sigma) = P'(\lambda, \theta) \cdot V(\sigma) \qquad (3)$$

where $\dot{Q}'$ is the latent heat rate per unit mass, and $P'$ is the precipitation. The form $V(\sigma) = \sigma^4 \sin(\pi\sigma)$ fits the GCM's heating fairly well. The vertical profile obtained from this functional form is shown in Fig. 13. The maximum heating occurs at the 830 mb level and decreases both upward and downward. Above 205 mb and at the surface, it is virtually zero.

The linear model responses to the heating distribution (3) are shown in Figs. 14a–f for geopotential height anomaly at 205, 515, and 990 mb and temperature anomaly at 515, 830, and 990 mb levels. The results in Fig. 14 are very similar to the sum of the response to sensible and latent heating. The temperature anomalies at all three levels compare rather well with the corresponding GCM results shown in Fig. 5, although the low level temperatures are somewhat stronger in Fig. 14. Thus, given the precipitation distribution, one is able to use the linear model to predict the atmospheric response to midlatitude SST anomaly.

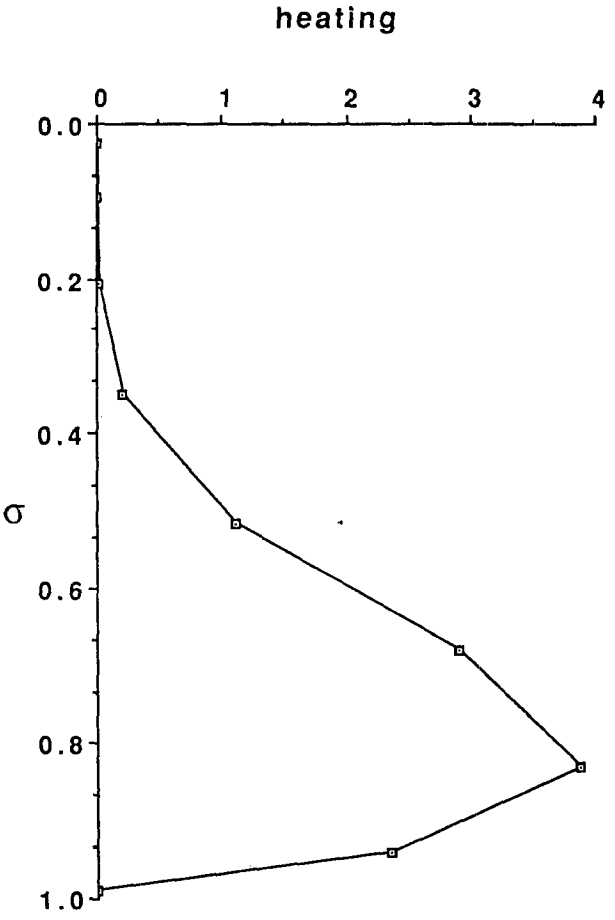


FIG. 13. Idealized vertical heating profile obtained from the functional form $\sigma^4 \sin\pi\sigma$, while keeping the vertically integrated positive part of the heating unchanged in the positive anomaly case.

The results are found to be insensitive to the precise form of $V(\sigma)$ as long as it remains shallow.

*b. Moisture budget*

Our next goal is to relate the precipitation anomaly to the SST anomaly. The moisture balance equation of the GCM in $\sigma$-coordinates reads:

$$\frac{dq}{dt} = S \qquad (4)$$

or

$$\frac{\partial q}{\partial t} + \nabla \cdot (\mathbf{V}q) + \frac{\partial(\dot{\sigma}q)}{\partial \sigma} - q\nabla \cdot \mathbf{V} - q\frac{\partial \dot{\sigma}}{\partial \sigma} = S \qquad (5)$$

where $q$ is the mixing ratio and $S$ is the moisture source or sink; all other symbols are standard. The GCM's continuity equation in $\sigma$-coordinate reads:

$$\frac{\partial \dot{\sigma}}{\partial \sigma} = -\frac{\partial \ln p_s}{\partial t} - \mathbf{V} \cdot \nabla \ln p_s - \nabla \cdot \mathbf{V}, \qquad (6)$$

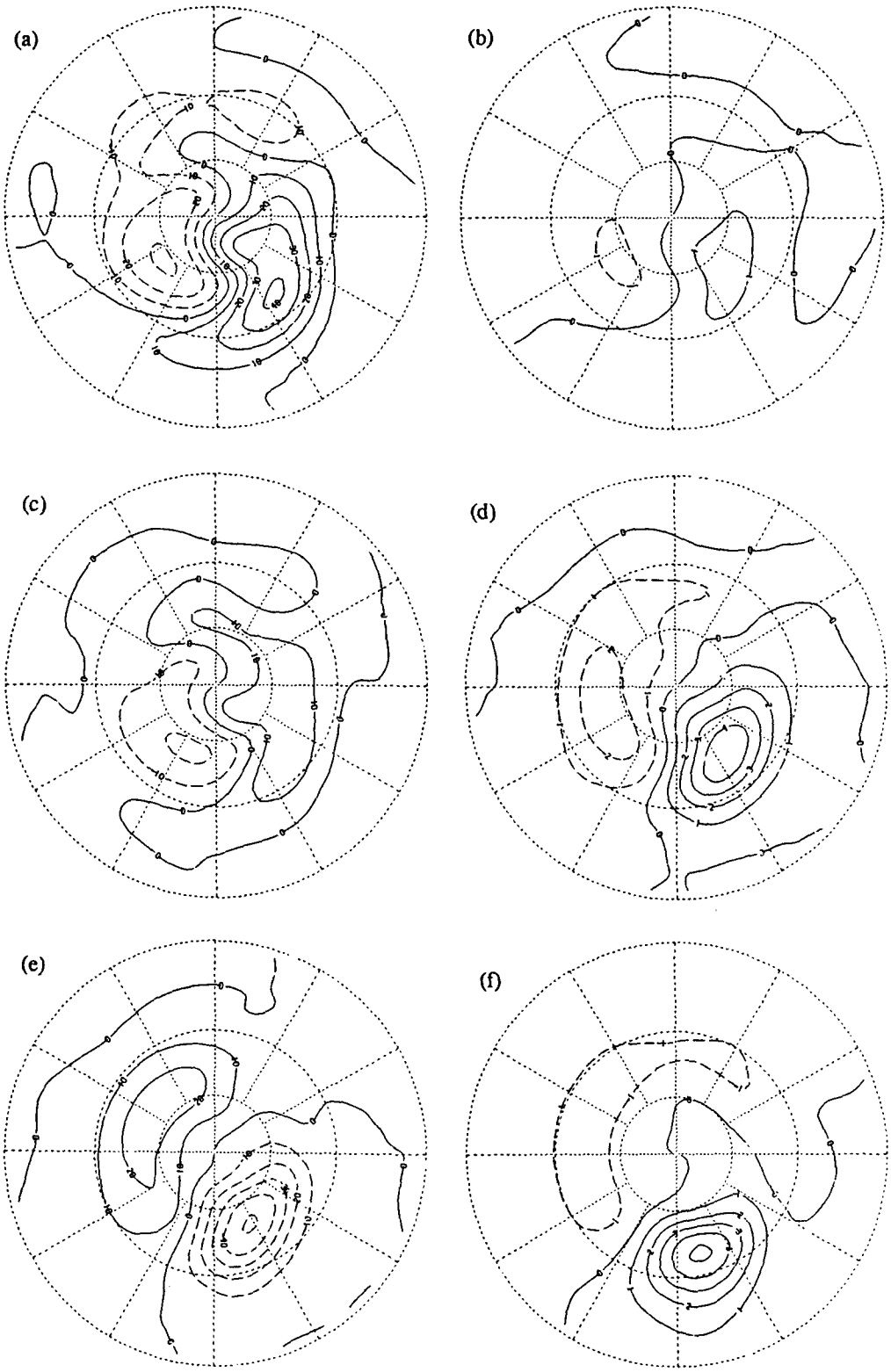


FIG. 14. Eddy geopotential height at (a) 205 mb, (b) 515 mb, and (c) 990 mb and eddy temperature at (e) 515 mb, (d) 830 mb, and (f) 990 mb obtained from the linear model with thermal diffusion and Newtonian cooling, when it is forced by precipitation anomaly with uniform vertical structure shown in Fig. 13 in a positive anomaly case. Contour intervals are 10 gpm in (a), (b), and (c) and 1 K in (d), (e), and (f); positive contours are solid and negative ones are dashed.

where $p_s$ is the surface pressure. Combining (5) and (6), taking a time average, one gets:

$$\nabla\cdot(\bar{\mathbf{V}}\bar{q}) + \nabla\cdot(\overline{\mathbf{V}'q'}) + \frac{\partial(\bar{\sigma}\bar{q})}{\partial\sigma} + \frac{\partial(\overline{\dot{\sigma}'q'})}{\partial\sigma} + \bar{q}\bar{\mathbf{V}} \times \nabla\overline{\ln p_s} + \{\overline{q\mathbf{V}}\cdot\nabla\overline{\ln p_s} - \bar{q}\bar{\mathbf{V}}\cdot\nabla\overline{\ln p_s}\} = S. \quad (7)$$

Vertically integrating (7) over the whole column, one gets the following moisture budget:

$$M + T = P - E \quad (8)$$

where

$$M = -\frac{p_s}{g}\int_0^1 \nabla\cdot(\bar{\mathbf{V}}\bar{q})d\sigma$$

$$T = -\frac{p_s}{g}\int_0^1 \nabla\cdot(\overline{\mathbf{V}'q'})d\sigma$$

Here $E$ is the evaporation, and $P$ the precipitation. Since the mean moisture flux convergence ($M$) can be calculated from the GCM time mean flow, and evaporation and precipitation are known from GCM data, the transient moisture contribution ($T$) is then computed as a residual of the moisture budget equation (8). [In (8), the terms associated with log surface pressure have been neglected due to the small contribution.]

The horizontal distributions of precipitation minus evaporation, mean, and transient moisture flux convergence are shown in Figs. 15a,b, and c, respectively. As we have seen in Fig. 2, the rainfall anomaly is shifted northeastward from the evaporation maximum in this model. To appreciate the significance of this shift, we note that the magnitude of the difference between precipitation and evaporation is comparable to the anomalous precipitation itself. The mean moisture flux convergence shows an east–west dipole structure, which causes the eastward shift in Fig. 15a. This term can be separated further into mean advection and divergence contributions. Apparently, advection is the main cause for the east–west dipole structure in Fig. 15b. The northward shift in Fig. 15a, however, is caused by the transient moisture flux convergence shown in Fig. 15c. All three terms in the balance are comparable, with the transient moisture contribution being slightly weaker. Several possible approximations can be made for the precipitation,

$$P \approx E \quad (9)$$

$$P \approx E + M \quad (10)$$

$$P \approx E + T. \quad (11)$$

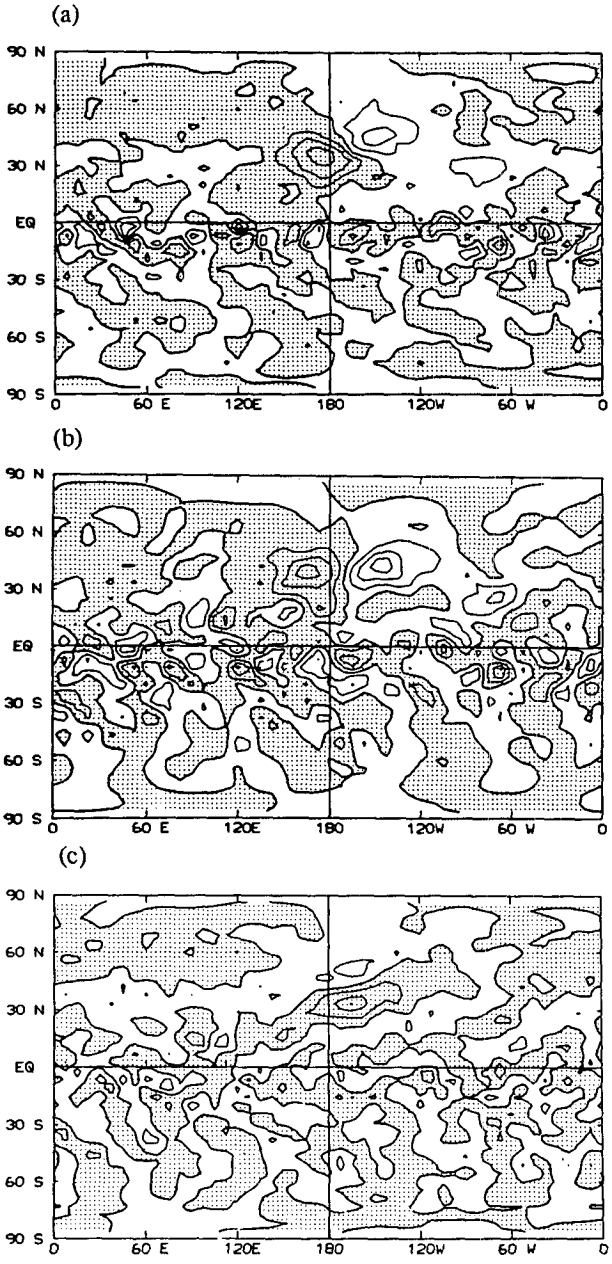


FIG 15. The horizontal distribution of precipitation minus evaporation (a), vertically integrated mean moisture flux convergence (b), and vertically integrated transient moisture flux convergence (c) in the positive anomaly case. Contour interval is $5 \times 10^{-6}$ kg s$^{-1}$ m$^{-2}$ (which is equivalent to ~0.043 cm day$^{-1}$); negative values are shaded.

The left of Fig. 16 contains the linear model responses at 205 mb to various heating distributions when taking the approximated precipitation as in (9)–(11) and utilizing the vertical distribution shown in Fig. 13. The differences between the left panels of Fig. 16 and the response to the GCM precipitation are shown on the right of Fig. 16. As one might expect, the linear model response to precipitation as approximated by evaporation is stronger in general and the center position has been dislocated, in comparison to the response to GCM precipitation (Fig. 14a). When the precipitation is approximated by evaporation plus mean and evaporation plus transient moisture flux convergences, both show some degree of improvement,

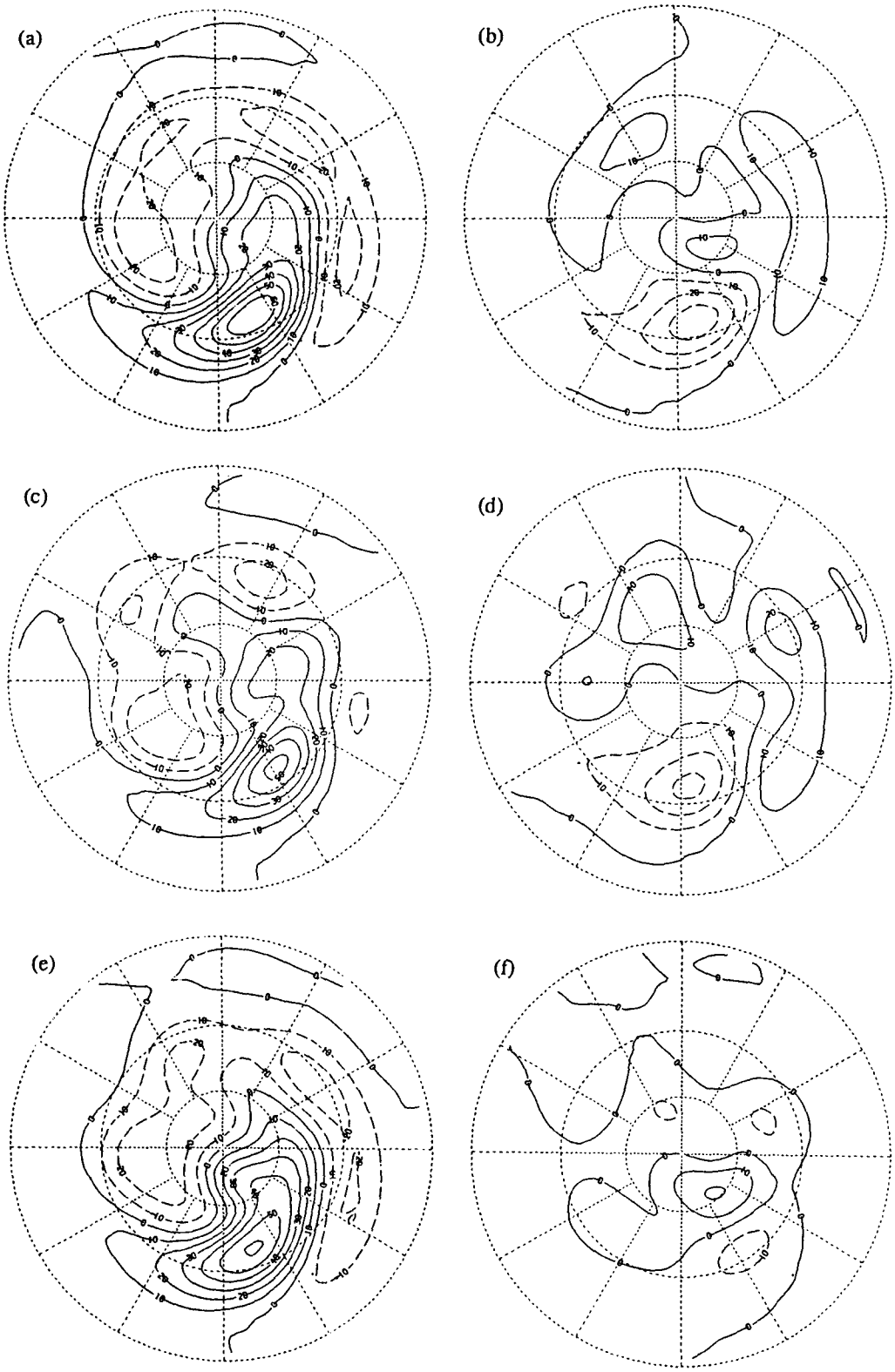


FIG. 16. Linear model (with thermal diffusion and Newtonian cooling) eddy geopotential height at 205 mb forced by (a) evaporation anomaly, (b) precipitation minus evaporation, (c) evaporation plus mean moisture flux convergence, (d) mean moisture convergence, (e) evaporation plus transient moisture flux convergence, and (f) transient moisture flux convergence in positive anomaly case, with uniform vertical distribution shown in Fig. 13. Contour interval is 10 gpm; positive contours are solid and negative ones are dashed.

with the former being closer to Fig. 14a. By comparing the three difference patterns on the right, one finds similar structure to that seen in Fig. 15. However, it is evident that mean moisture flux convergence is the main cause for the difference between the response to GCM precipitation and that to precipitation as approximated by evaporation.

*c. Latent heat parameterization*

According to (10), to relate the precipitation to the ocean surface temperature, one has to parameterize the evaporation and the mean moisture flux convergence $-\nabla\cdot(\bar{\mathbf{V}}\bar{q})$ (we ignore the effect of transients). As the first step, we write the mean moisture flux convergence in terms of zonal mean and perturbation as follows:

$$\{-\nabla\cdot\bar{\mathbf{V}}\bar{q})\}^* = -\nabla\cdot([\bar{\mathbf{V}}]\bar{q}^* + \bar{\mathbf{V}}^*[\bar{q}]). \quad (12)$$

Here we define '[ ]' as zonal mean and '*' as the deviation from that zonal mean. We ignore terms that involve second-order perturbations in (12) to be consistent with the linear model.

The first time in (12), the mean moisture flux convergence due to the zonal mean wind $-\nabla\cdot([\bar{\mathbf{V}}]\bar{q}^*)$, is found to be dominant; the contribution from the mean moisture flux convergence due to the perturbation wind field $-\nabla\cdot(\bar{\mathbf{V}}^*[\bar{q}])$ is less important. The second term is relatively easy to incorporate in the linear model, since $[\bar{q}]$ is assumed given by the basic state. However, since the linear model does not have a moisture equation, one has to relate the moisture perturbation with the temperature perturbation. To achieve this, we assume that the relative humidity is a constant. The mixing ratio $q$ is defined as

$$q = rq_s(T) \approx 0.622\, r\frac{e_s(T)}{P} \quad (13)$$

where $r$ is the relative humidity and $e_s(T)$ the saturation vapor pressure. In the following discussion, $r$ is fixed as a constant and $e_s(T)$ is obtained from the Clausius–Clapeyron equation,

$$e_s(T) = C(T)e^{-m_v L_c/R^* T}.$$

Linearizing (13) about the zonal mean state, one can get the perturbation mixing ratio,

$$q^* = 0.622r\frac{1}{P}\frac{de_s}{dT}([T])T^*. \quad (14)$$

We use (14) to compute the GCM's mixing ratio at all levels. The relative humidity can be obtained from GCM data and we zonally average the data between 30° and 40°N to get the following values at different levels: 0.0, 0.0, 0.4, 0.6, 0.6, 0.6, 0.7, 0.85, 0.9. The zonal mean mixing ratio is calculated from (13) using the zonal mean temperature. The zonally asymmetric part of the mean moisture flux convergence $-\nabla\cdot(\bar{\mathbf{V}}\bar{q})$ is then calculated from (12). The vertically integrated

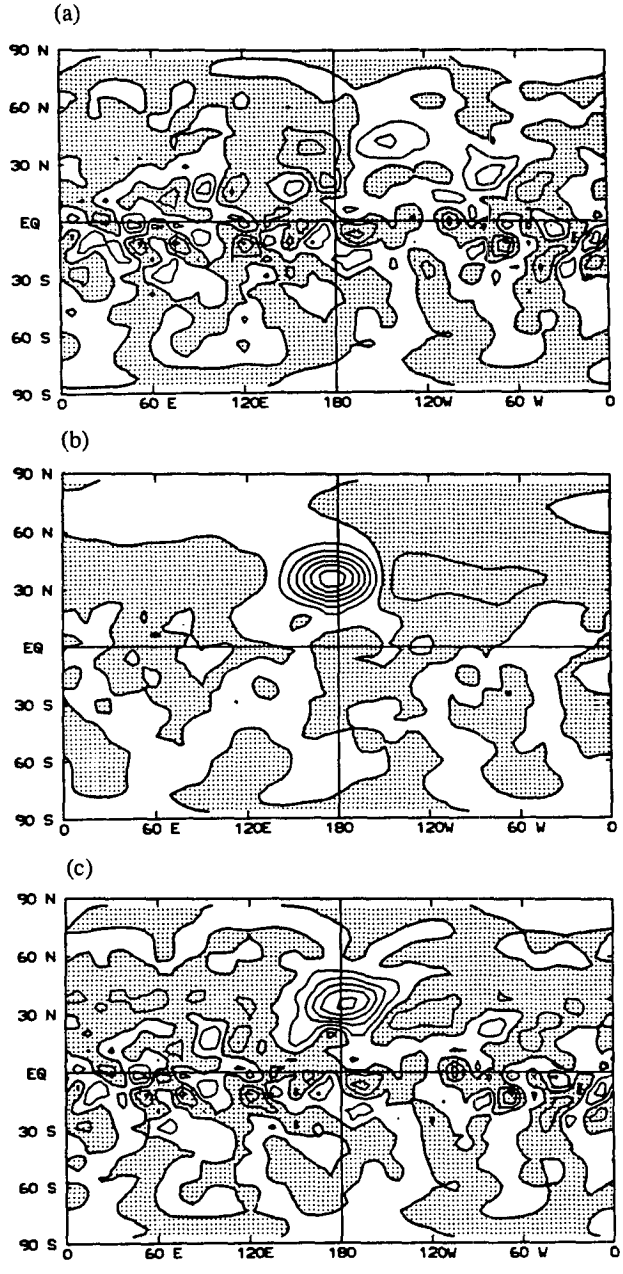


FIG. 17. (a) Mean moisture flux convergence obtained when GCM's perturbation mixing ratio is estimated from Eq. (14) with GCM's temperature perturbation; (b) perturbation evaporation estimated from Eq. (15); (c) the sum of (a) and (b). Contour interval is $5 \times 10^{-6}$ kg s$^{-1}$ m$^{-2}$; negative values are shaded.

mean moisture flux convergence as calculated in this way is shown in Fig. 17a. Comparing this with that calculated from GCM mixing ratio data (Fig. 15b), one finds the pattern looks approximately correct, but the amplitude is reduced by 30%.

The second step is to relate the evaporation anomaly to the temperature anomaly. This is more difficult since the evaporation can depend strongly on the surface wind. When one ignores the surface wind dependence of evaporation and mimics the GCM's evaporation anomaly by the moisture difference between ocean surface and lower atmosphere,

$$E^* = c_E(q_s^* - q_9^*), \tag{15}$$

the evaporation anomaly obtained is shown in Fig. 17b. Both $q_s^*$ and $q_9^*$ are calculated from (14). The value of $c_E$ is chosen by computing the ratio between the zonal mean evaporation and the zonal mean air–sea surface mixing ratio difference, which is approximately $1.5 \times 10^{-6}$ kg s$^{-1}$ m$^{-2}$. The meridional scale of the evaporation in Fig. 17b is broader than that in Fig. 2e. Other than that, Fig. 17b compares very well with the GCM evaporation.

Combining the above discussions, we finally get the following latent heat parameterization,

$$\dot{Q}^* = V(\sigma)\left[c_E(q_s^* - q_9^*) + \frac{p_s}{g}\int_0^1 [u](\sigma)\frac{\partial q^*(\sigma)}{\partial x}\,d\sigma\right], \tag{16}$$

where $q^*$ is related to $T^*$ by (14). When using the GCM's temperature and zonal mean zonal wind, we get the parameterized rainfall anomaly in Fig. 17c.

When the latent heating formulation (16) is used in the linear model, the temperatures will be coupled between different vertical levels. In the linear model used here, the temperature perturbation at one level can only be coupled to its nearest neighbors (TH). This prevents the direct application of (16) into the linear model. Instead of reconstructing the model, we solve this problem by iteration.

Two calculations have been performed using the linear model. The first one uses a heating proportional to the air-sea moisture difference, that is, it only includes the evaporation (the first term) in (16). The second calculation uses the full form of (16). Both iterations converge very fast towards the solution. The eddy geopotential height at 205, 515, and 990 mb levels obtained from the two iterations is shown in Fig. 18. The eddy temperatures are shown in Fig. 19 at 515, 830, and 990 mb levels. The response to parameterized evaporation is quite accurate as compared with the response to the GCM evaporation. The predicted evaporation is shown in Fig. 20. The overall pattern is quite similar to the GCM evaporation shown in Fig. 2e, but it underestimates it ($\sim$0.20 cm day$^{-1}$ in Fig. 20 and 0.28 cm day$^{-1}$ in Fig. 2e) and shows some unrealistic structures in the tropics. If one averages the GCM's evaporation anomaly in the positive and the negative anomaly cases (Figs. 2e and f), one would get an amplitude about the same as in Fig. 20. This suggests that the linear Clausius–Clapeyron equation underestimates the evaporation in the positive case and overestimates it in the negative case.

Adding the mean moisture advection term in the iteration procedure, we find the following improvements: the amplitude of the eddy geopotential height at all levels is reduced and the center position has been shifted eastward, and the eddy temperature anomaly is also greatly reduced in amplitude at all three levels. The main feature of the linear model response to the precipitation anomaly in Fig. 14 are well captured by the response to parameterized precipitation on the right of Fig. 18. Differences are mainly that the whole pattern in Fig. 18 is shifted westward and the negative center in the upper troposphere is not well simulated. However, it is still quite impressive that one can get basically the correct response just from the SST anomaly and the zonal mean basic state.

The above latent heat parameterization explains how a midlatitude SST anomaly can directly induce the precipitation anomaly and then the thermally forced waves in the atmosphere. In reality, the thermally forced waves will further interact with the climatological stationary waves, modify the storm track eddy activities, and finally strengthen the wave responses. It is a much more complicated picture when significant storm track displacement takes place. However, to understand the direct thermal response to a SST anomaly is a necessary first step towards the understanding of the full processes.

## 6. Conclusions

The stationary wave response to a fixed midlatitude SST anomaly in an idealized GCM has been examined. The zonally symmetric control climate is perturbed by a monopolar SST anomaly centered at 40°N. One positive and one negative anomaly experiment have been conducted. The magnitude of the rainfall anomaly in the positive case is three times stronger than in the negative case. However, the amplitude of the stationary response is only one and half times as strong and with opposite sign in the positive case in comparison to the negative case.

Despite the significant differences between the responses in the idealized GCM experiments discussed in this paper and in the more realistic GCMs, the idealized GCM provides a simple framework for the study of fundamental aspects of the air–sea interaction problem. Using the linear steady baroclinic model devel-

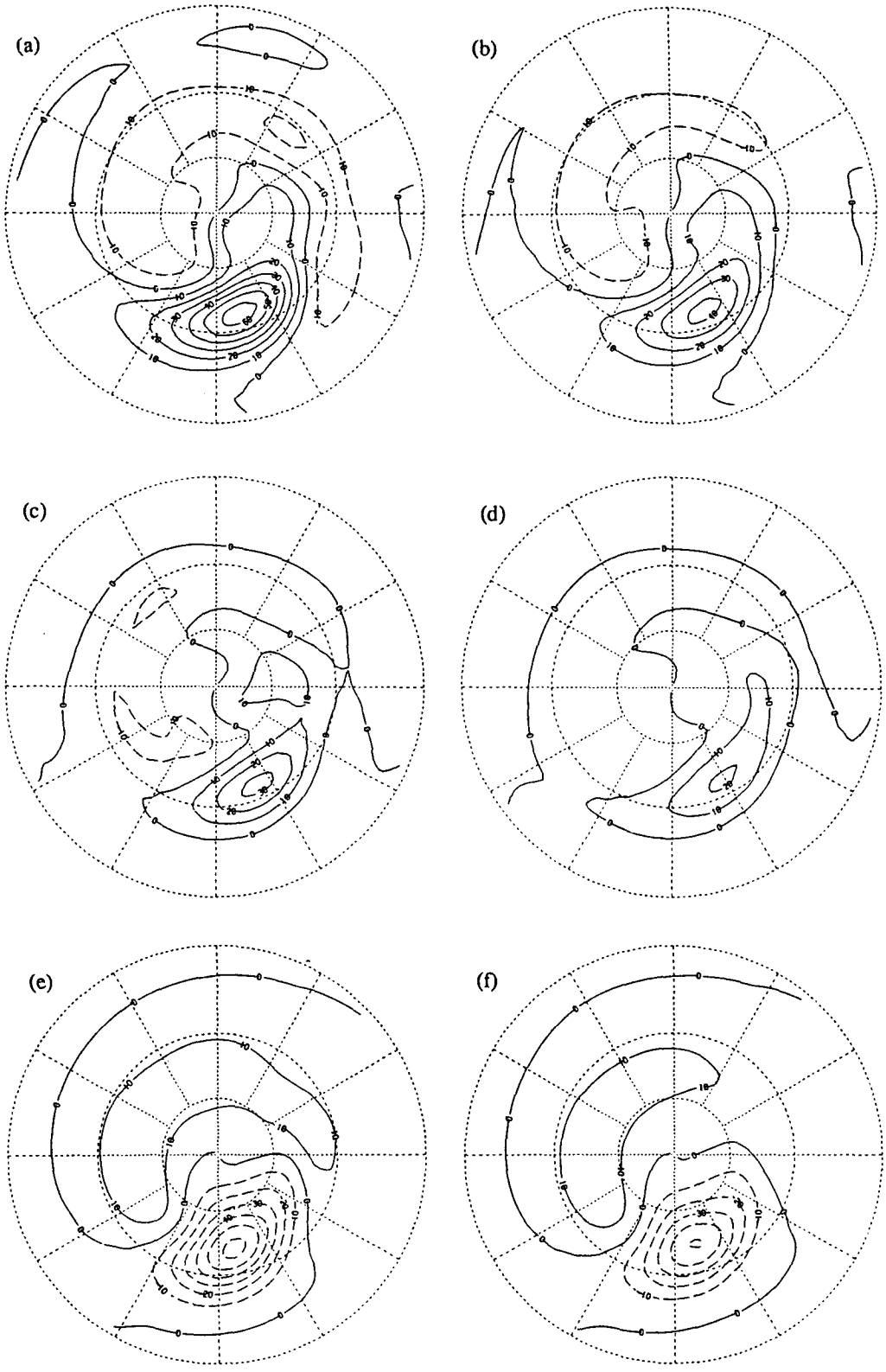


FIG. 18. Linear model (with diffusion and Newtonian cooling) eddy geopotential height at 205, 515, 990 mb levels forced by evaporation anomaly parameterized as Eq. (15) (a, c, and e) and forced by evaporation plus mean moisture advection as parameterized in Eq. (18) (b, d, and f). Contour interval is 10 gpm; positive contours are solid and negative ones are dashed.

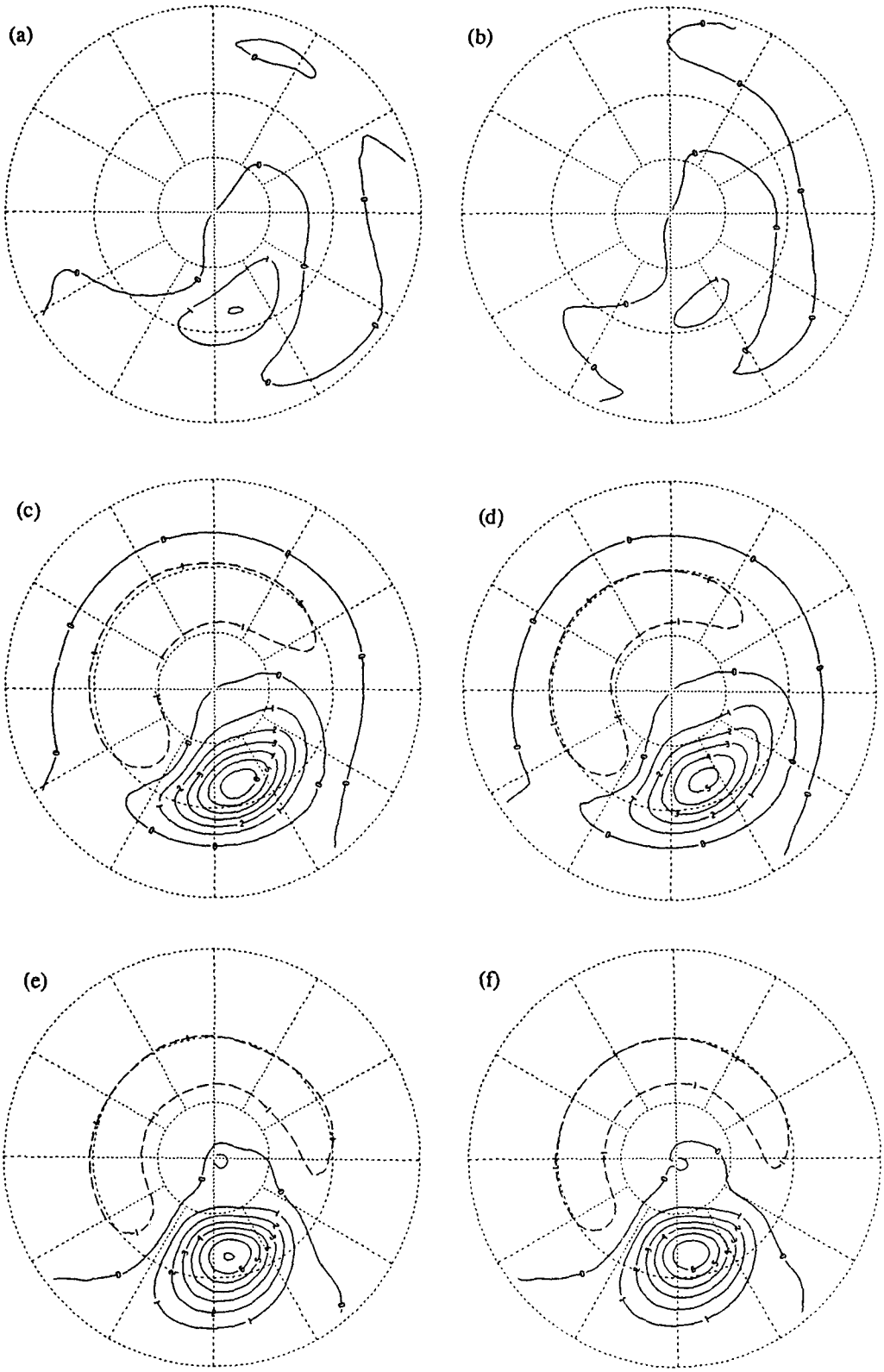


FIG. 19. Same as Fig. 18, but for eddy temperature at 515, 830, and 990 mb levels.

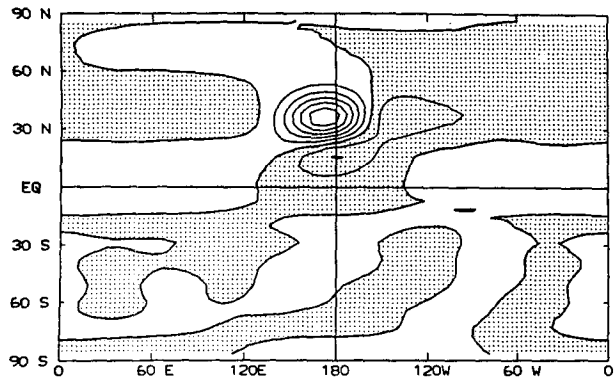


FIG. 20. Evaporation anomaly predicted by the linear model when it is parameterized as proportional to the air–sea surface mixing ratio difference. Contour interval is $5 \times 10^{-6}$ kg s$^{-1}$ m$^{-2}$. Negative values are shaded.

oped by Ting (1990) and Ting and Held (1990), we have found:

- Latent heating is the dominant forcing in the idealized GCM except for the temperature field near the surface.
- The vertical structure of this heating is very shallow (maximum at around 940 mb in this case).
- Sensible heating can be parameterized as a simple damping of the boundary atmospheric temperature perturbation towards the sea surface temperature perturbation.
- The transients play two distinct roles in determining the responses: low-level transient eddy heat fluxes act to damp the lower-level temperature signal (one must include damping that mimics this effect in order to produce useful results with the linear model); and the transient eddy flux of moisture displaces the heating anomaly poleward, where it forces a somewhat different atmospheric response than it would if the heating occurred directly above the evaporation anomaly.
- The transient eddy flux momentum in upper troposphere is relatively unimportant compared with the heating, however, it still forces a modest northward shift of the atmospheric responses similar to that due to the transient moisture fluxes.

In the realistic GCM case, it is possible that the anomalous momentum transients become dominant and make the other forcing less important. However, it is still necessary to understand the thermal forcing as a first approximation. A large shift in the storm track position may occur in a realistic GCM due to the feedback between the thermally forced anomaly wave and the transient eddies. But one still has to understand the thermally forced stationary wave that initiates the feedback processes.

Since the linear model response is not very sensitive to the vertical structure of the heating as long as the maximum heating is below 800 mb, the precipitation is the only piece of data one needs to compute the atmospheric responses. The precipitation anomaly, in turn, is mainly determined by the evaporation anomaly and mean moisture advection. The latter can be included in the linear calculation by assuming that relative humidity is fixed, while the evaporation can simply be set proportional to the air–sea mixing ratio difference. With these approximations, one can derive the atmospheric response directly from the SST anomaly itself.

While this relatively simple picture seems to hold in this idealized GCM, we do not think that it holds in the atmosphere or in more realistic GCMs. One needs to fully understand the interaction between the precipitation field and the thermally forced wave, the climatological stationary wave, and the transient eddies in order to accomplish the goal of understanding how the atmospheric anomaly is controlled by the SST anomaly.

*Acknowledgments.* This work was carried out while the author was a student at Princeton University. Dr. I. M. Held, as the author's thesis advisor, contributed continuing support and guidance throughout this study. The author wishes to also acknowledge Drs. M. L. Blackmon, N.-C. Lau, and H. Nakamura for their comments on the manuscript. The author was supported by NOAA Grant NA87EAD00039 at Princeton University.

## REFERENCES

Blackmon, M. L., J. M. Wallace, N.-C. Lau and S. L. Mullen, 1977: An observational study of the Northern Hemisphere wintertime circulation. *J. Atmos. Sci.*, **34**, 1040–1053.

Frankignoul, C., 1985: Sea surface temperature anomalies, planetary waves, and air–sea feedback in the middle latitudes. *Rev. Geophys.*, **23**, 357–390.

Gordon, C. T., and W. F. Stern, 1982: A description of the GFDL global spectral model. *Mon. Wea. Rev.*, **110**, 625–644.

Held, I. M., 1983: Stationary and quasi-stationary eddies in the extratropical troposphere: Theory. *Large-Scale Dynamical Processes in the Atmosphere*, B. J. Hoskins and R. P. Pearce, Eds., Academic Press, 127–168.

Hoskins, B. J., 1983: Modeling of the transient eddies and their feedback on the mean flow. *Large-Scale Dynamical Processes in the Atmosphere*, B. J. Hoskins and R. P. Pearce, Eds., Academic Press, 169–199.

——, and D. J. Karoly, 1981: The steady linear response of a spherical atmosphere to thermal and orographic forcing. *J. Atmos. Sci.*, **38**, 1179–1196.

Lau, N.-C., 1979: The structure and energetics of transient disturbances in the Northern Hemisphere wintertime circulation. *J. Atmos. Sci.*, **36**, 982–995.

——, and M. J. Nath, 1990: A general circulation model study of the atmospheric response to extratropical SST anomalies observed in 1950–79. *J. Climate*, **3**, 965–989.

Lindzen, R. S., and S. Nigam, 1987: On the role of sea surface temperature gradients in forcing low-level winds and convergence in the tropics. *J. Atmos. Sci.*, **45**, 2440–2458.

Manabe, S., D. G. Hahn and J. L. Holloway, 1979: Climate simulation with GFDL spectral models of the atmosphere. GARP Publ. Ser. No. 22, WMO, Geneva,

Namias, J., 1959: Recent seasonal interactions between north Pacific

waters and the overlying atmospheric circulation. *J. Geophys. Res.*, **64**, 631–646.

——, 1963: Large-scale air–sea interactions over the north Pacific from summer 1962 through the subsequent winter. *J. Geophys. Res.*, **68**, 6171–6186.

——, 1969: Seasonal interactions between the north Pacific Ocean and the atmosphere during the 1960's. *Mon. Wea. Rev.*, **97**, 173–192.

——, and D. R. Cayan, 1981: Large scale air–sea interactions and short-period climatic fluctuations. *Science*, **214**, 869–876.

Palmer, T. N., and Z.-B. Sun, 1985: A modeling and observational study of the relationship between sea surface temperature in the northwest Atlantic and the atmospheric general circulation. *Quart. J. Roy. Meteor. Soc.*, **111**, 947–975.

Pitcher, E. J., M. L. Blackmon, G. T. Bates and S. Munõz, 1988: The effect of north Pacific sea surface temperature anomalies on the January climate of a general circulation model. *J. Atmos. Sci.*, **45**, 173–188.

Ratcliffe, R. A. S., and R. Murray, 1970: New lag associations between North Atlantic sea temperature and European pressure applied to long-range weather forecasting. *Quart. J. Roy. Meteor. Soc.*, **96**, 226–246.

Simmons, A. J., and B. J. Hoskins, 1978: The life cycles of some nonlinear baroclinic waves. *J. Atmos. Sci.*, **35**, 414–432.

Ting, M., 1990: The stationary wave response to tropical and mid-latitude SST anomalies. Ph.D thesis, Princeton University.

——, and I. M. Held, 1990: The stationary wave response to a tropical SST anomaly in an idealized GCM. *J. Atmos. Sci.*, **47**, 2546–2566.

Wallace, J. M., and Q.-R. Jiang, 1987: On the observed structure of the interannual variability of the atmosphere–ocean climate system. *Atmospheric and Oceanic Variability*, H. Cattle, Ed., Royal Meteor. Soc. 17–43.

——, C. Smith and Q.-R. Jiang, 1990: Spacial patterns of atmosphere–ocean interaction in the Northern Winter. *J. Climate*, **3**, 990–998.